

On the noise prediction for serrated leading edges

B. Lyu¹ † and M. Azarpeyvand²

¹Department of Engineering, University of Cambridge, Cambridge CB2 1PZ, UK

²Department of Mechanical Engineering, University of Bristol, Bristol BS8 1TR, UK

(Received ?; revised ?; accepted ?. - To be entered by editorial office)

An analytical model is developed for the prediction of noise radiated by an aerofoil with leading edge serration in a subsonic turbulent stream. The model makes use of the Fourier Expansion and Schwarzschild techniques in order to solve a set of coupled differential equations iteratively and express the far-field sound power spectral density in terms of the statistics of incoming turbulent upwash velocity. The model has shown that the primary noise reduction mechanism is due to the destructive interference of the scattered pressure induced by the leading edge serrations. It has also shown that in order to achieve significant sound reduction, the serration must satisfy two geometrical criteria related to the serration sharpness and hydrodynamic properties of the turbulence. A parametric study has been carried out and it is shown that serrations can reduce the overall sound pressure level at most radiation angles, particularly at downstream angles close to the aerofoil surface. The sound directivity results have also shown that the use of leading edge serration does not particularly change the dipolar pattern of the far-field noise at low frequencies, but it changes the cardioid directivity pattern associated with radiation from straight-edge scattering at high frequencies to a tilted dipolar pattern.

1. Introduction

The issue of noise generation from aerofoils has been the subject of much theoretical, experimental and computational research over the past few decades and is of great importance in many applications, such as jet engines, wind turbine blades, high-speed propellers, helicopter blades, etc. Aerofoil noise can generally be categorised as self-noise and inflow-turbulence noise. The aerofoil self-noise is due to the interaction of the aerofoil with its own boundary layer and the flow instabilities present in the boundary layer (Brooks *et al.* 1989). The aerofoil inflow-turbulence noise, on the other hand, is due to the interaction of an incoming unsteady gust with the aerofoil. The aerofoil inflow-turbulence interaction noise is a significant contributor in systems involving multiple rows of blades, such as jet engines and contra-rotating propellers. For instance, the wake flow shed by the aircraft engine fan blades interacts with following blades and vanes, causing leading edge noise from the rear blades. Likewise, the interaction of the wake flow from the front row blades in a contra-rotating open rotor (CROR) system with the downstream blades is considered as the main source of broadband noise from such configurations. Also, the interaction of atmospheric turbulence with the blades of wind turbines can also cause high level of low-frequency broadband noise.

The prediction of leading-edge turbulence interaction noise has been the subject of much research over the past decades (Sears 1941; Graham 1970; Amiet 1975; Devenport *et al.* 2010). Sears originally considered the interaction of an unsteady sinusoidal gust

† Email address for correspondence: bl362@cam.ac.uk

with a flat plate and developed a model for the prediction of the plate aerodynamic response under such unsteady loading. Sears' model was later further developed and extended to compressible flows by [Graham \(1970\)](#) and [Amiet \(1975\)](#). In Amiet's model, the blade response function to an incoming gust is first obtained using the Schwarzschild technique and the far-field sound is then formulated based on the theories of Kirchoff and [Curle \(1955\)](#) using the radiation integral. Amiet's model shows that the far-field sound power spectral density (PSD) is directly related to the energy spectrum of the velocity fluctuations of the incoming gust. It has been widely shown that Amiet's model can provide fairly good comparisons with experimental observations when the turbulence statistical quantities are known. The effects of aerofoil geometrical parameters, such as angle of attack, aerofoil thickness, camber, etc. on the generation of leading-edge turbulence interaction noise has also been the subject of some theoretical works ([Goldstein & Atassi 1976](#); [Goldstein 1978](#); [Myers & Kerschen 1995, 1997](#); [Atassi *et al.* 1993](#); [Devenport *et al.* 2010](#); [Roger & Carazo 2010](#)).

The use of leading-edge treatments, inspired by the flippers of humpback whales ([Bushnell & Moore 1991](#); [Fish & Battle 1995](#); [Miklosovic & Murray 2004](#); [Fish *et al.* 2008](#); [Pedro & Kobayashi 2008](#)) has been shown to lead to improved aerodynamic and hydrodynamic performance, particularly at high angles of attack. The recent extensive experimental works on the effects of leading-edge serrations on the generation and control of turbulence interaction noise has shown that the use of such treatments can result in significant noise reduction over a wide range of frequencies ([K. Hansen & Doolan 2012](#); [Narayanan *et al.* 2015](#)). For example, [Narayanan *et al.* \(2015\)](#) showed that using sinusoidal leading-edge serrations for a flat plate and NACA-65 type aerofoil leads to significant noise reduction. Noise reductions were found to be significantly higher for the flat plates. It was also shown that the sound power reduction level is more sensitive to the serration amplitude and less sensitive to the serration wavelength. In a more recent study, it was shown that the use of complex leading-edge serrations, i.e. serrations formed from the superposition of two serration profiles of different frequency, amplitude and phase, can produce greater noise reductions than single wavelength serrations ([Chaitanya *et al.* 2016](#)).

Besides the experimental activities, the problem of leading-edge noise reduction using wavy edges has recently been studied in several computational works ([Lau *et al.* 2013](#); [Kim *et al.* 2016](#); [Turner & Kim 2016](#)). In the work of [Lau *et al.* \(2013\)](#), the effectiveness of leading edge serrations for turbulence interaction noise reduction was examined numerically. It was found that the hydrodynamic quantity $k_1 h$ plays an important role in determining the effectiveness of the serration, where k_1 is the hydrodynamic wavenumber of the disturbance in the streamwise direction and the serration root-to-tip distance is $2h$. The serration wavelength λ , on the other hand, was found to be less important. However, one should note that the study assumed a perfect coherence in the spanwise direction, which may not be the case in real-world applications. The three-dimensionality of the disturbance was accounted for in the work of [Kim *et al.* \(2016\)](#) using synthetically generated turbulence. It was argued that both a source cut-off and destructive interference effects contributed to the sound reduction. Both of these two numerical works used a regular sinusoidal serration profile attached to a flat plate. In a more recent work by [Turner & Kim \(2016\)](#), a dual-frequency wavy serration profile was proposed and it was found that the more complex serration geometries can increase the noise reduction. It is again worth noting that the upstream disturbance was assumed to be perfectly correlated in the spanwise direction.

The above discussion provided a comprehensive literature review for the use of leading edge serrations as a passive method for reduction of aerofoil inflow-turbulence interaction noise. It is, however, worth mentioning that the topic of leading edge serrations

for improving the aerodynamic performance of aerofoils has attracted much attention over the past few decades. A great deal of experimental and numerical studies have been conducted to investigate the effects of leading edge modifications on the aerofoil aerodynamic forces, early separation and stall behaviour, unsteady forces, etc., at different flow regimes. The detailed literature review of the aerodynamic performance of serrated aerofoils is beyond the scope of the current study, but interested readers are referred to several works (Johari *et al.* 2007; Hansen *et al.* 2011; Miklosovic & Murray 2004).

Despite the significant body of work on noise reduction using leading-edge serrations, no mathematical model has yet been developed to relate the radiated noise to the serration geometrical parameters and turbulence quantities. While the experimental observations (Paterson & Amiet 1976; Roger & Carazo 2010; Roger *et al.* 2013; Narayanan *et al.* 2015) and computational works (Allampalli *et al.* 2009; Atassi *et al.* 1993; Gill *et al.* 2013; Hixon *et al.* 2006; Lau *et al.* 2013; Kim *et al.* 2016; Turner & Kim 2016) have provided the evidence that leading-edge serrations can lead to significant noise reduction, an accurate and robust analytical model can help better understand the mechanism of such noise reductions. An accurate analytical model will also enable us to assess the effectiveness of leading edge serrations at high Mach numbers and Reynolds numbers, relevant to turbomachinery applications, where numerical approaches are very costly and experiments difficult. This will also provide us with a tool for blade design optimization purposes. In this paper, we aim to extend Amiet’s leading-edge noise prediction model to the case of serrated leading-edges and provide a parametric study for the effects of serrations on far-field noise. It will be shown in Section II that the introduction of the serration will lead to a complex differential equation, which is solved using the Schwarzschild technique in an iterative manner. The scattered pressure loading will then be used in a radiation integral and the far-field PSD will be found in terms of the incoming gust statistical quantities and blade response function. Section III presents an extensive parametric study of the proposed model and results will be provided for far-field sound pressure level, noise directivity and overall sound pressure level. The noise reduction mechanism will also be discussed in this section. Section IV concludes the paper and lists our future plans.

2. Analytical formulation

In this section, we present a detailed derivation for the prediction of noise due to the interaction of an unsteady gust with a flat plate with serrated leading edge. The analytical model developed is based on Amiet’s model and Schwarzschild technique for solving the Helmholtz equation with appropriate boundary conditions.

2.1. Leading edge noise modelling

Let’s consider an infinitesimally thin flat plate with leading edge serrations, as shown in figure 1, with an averaged chord length c and spanwise length d . A Cartesian coordinate system is chosen such that the serration profile is an oscillatory function of zero mean. When the acoustic wavelength is smaller than the chord length c , the flat plate can be considered as an infinitely long plate without a trailing edge (Amiet 1976b, 1978; Roger & Moreau 2005). When the frequencies are high enough as to the semi-infinite simplification is permissible, the plate can also considered infinite in the spanwise direction when it has a relatively large aspect ratio, typically larger than 3 (Amiet 1978; Roger & Carazo 2010). Let x' , y' and z' denote the streamwise, spanwise and normal directions to the plate, respectively. The observer point is located at (x_1, x_2, x_3) , as shown in figure 1.

As mentioned above, the origin of the coordinate system (x', y', z') is chosen such that the serration profile, $H(y')$, is an oscillatory function of zero mean and that $H(y') = 0$

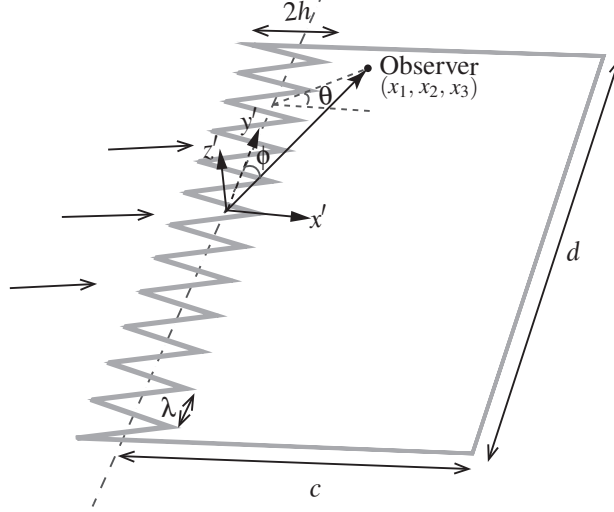


Figure 1: Schematic of a flat plate with a sawtooth-like leading edge.

in the absence of serrations. Though the method developed in this section can be used for any general periodic serrations, in this paper we only focus on sawtooth serration, as shown in figure 1, where the root-to-tip length is $2h$ and the serration wavelength is λ . The parameter $\sigma = 4h/\lambda$ will also be used to quantify the sharpness of the sawtooth serrations. To obtain a mathematical description of $H(y')$, let us consider a single sawtooth centred around the coordinate origin, and let (λ_0, ϵ_0) , (λ_1, ϵ_1) and (λ_2, ϵ_2) denote the three joint-points defining this single sawtooth, as shown in figure 2. The serration profile function $H(y')$ can therefore be defined as

$$H(y') = \begin{cases} \sigma_0(y' - \lambda_0 - m\lambda) + \epsilon_0, & \lambda_0 + m\lambda < y' \leq \lambda_1 + m\lambda \\ \sigma_1(y' - \lambda_1 - m\lambda) + \epsilon_1, & \lambda_1 + m\lambda < y' \leq \lambda_2 + m\lambda \end{cases}, \quad (2.1)$$

where $\sigma_j = (\epsilon_{j+1} - \epsilon_j)/(\lambda_{j+1} - \lambda_j)$, $j = 0, 1$ and $m = 0, \pm 1, \pm 2, \pm 3 \dots$.

In this paper, we focus our attention on the unsteady upwash disturbance (Amiet 1975), denoted by w , that exists upstream of the leading edge, convecting downstream with the mean flow at the speed of U . According to Kovaszny (1953), the unsteady motion on a uniform flow can be decomposed into vorticity, entropy and sound-wave modes. When perturbation amplitudes are small as to linearisation is permissible, the three modes are mutually independent. It is generally accepted that the incident turbulence can be well presented by vorticity mode, which convects at speed of the mean flow. Therefore, this study follows the same simplification and the incoming gust is assumed to be frozen in the frame moving with the mean flow, i.e. the velocity distribution is $w(x', y', t) = w_m(x' - Ut, y')$, where t denotes time, for some function $w_m(x_m, y_m)$ describing the distribution of upwash velocity in the travelling coordinate system $\{x_m, y_m, z_m\}$. In this paper we make use of the same assumption. In the plate fixed frame, the incoming gust can be written in terms of its wavenumber components, $\tilde{w}(k_1, k_2)$, as

$$w(x', y', t) = \iint_{-\infty}^{\infty} \tilde{w}(k_1, k_2) e^{i(k_1(x' - Ut) + k_2 y')} dk_1 dk_2, \quad (2.2)$$

where the Fourier components $\tilde{w}(k_1, k_2)$ is given by

$$\tilde{w}(k_1, k_2) = \left(\frac{1}{2\pi}\right)^2 \iint_{-L}^L w_m(x_m, y_m) e^{-i(k_1 x_m + k_2 y_m)} dx_m dy_m, \quad (2.3)$$

where L is a large but finite number to avoid convergence difficulties and k_1 and k_2 denote the Fourier wavenumbers in the streamwise and spanwise directions, respectively. Using (2.2) one can find

$$\begin{aligned} w(x', y', \omega) &= \frac{1}{2\pi} \int w(x', y', t) e^{i\omega t} dt \\ &= \frac{1}{U} \int_{-\infty}^{\infty} \tilde{w}(\omega/U, k_2) e^{i(\omega x'/U + k_2 y')} dk_2, \end{aligned} \quad (2.4)$$

where ω represents angular frequency.

Equation (2.4) suggests that the general unsteady gust can be decomposed into a set of plane-wave-like gusts, each of which taking the form of

$$w_i = w_{ia} e^{-i(\omega t - k_1 x' - k_2 y')}, \quad (2.5)$$

where, $k_1 = \omega/U$ and w_{ia} denotes the magnitude of the upwash velocity and is a function of both ω and k_2 . The scattered velocity potential ϕ_t is governed by the convective wave equation, i.e.

$$\nabla^2 \phi_t - \frac{1}{c_0^2} \left(\frac{\partial}{\partial t} + U \frac{\partial}{\partial x'} \right)^2 \phi_t = 0, \quad (2.6)$$

where c_0 denotes the speed of sound. Hence, if we can find the far-field sound induced by a single gust by solving the wave equation subject to appropriate boundary condition upstream of the leading edge and over the surface of the serrated plate, then a more general solution can readily be obtained by performing an integration over k_2 , as shown in (2.4). The next part of this section is therefore devoted to the single-gust solution for a flat plate with leading-edge serration.

2.2. Single-gust solution

The full solution ϕ_t to (2.6) can be written in terms of an initial and a residual potential part. The initial potential, ϕ_i , is used to cancel the upwash velocity on the plane $z' = 0$. Upon defining $k = \omega/c_0$, $\beta^2 = 1 - M_0^2$ and $M_0 = U/c_0$, one can show that on the plane $z' = 0$, ϕ_i takes the form of

$$\phi_i = -\Phi_{ia} e^{-i(\omega t - k_1 x' - k_2 y')}, \quad (2.7)$$

where $\Phi_{ia} \equiv -w_{ia} / \sqrt{(k_1 \beta + k M_0 / \beta)^2 + k_2^2 - (k/\beta)^2}$.

The Schwarzschild technique can then be used to calculate the second part, i.e. residual term, of the potential field, ϕ , which would cancel the potential field of the initial solution upstream of the leading edge (such that we have $\phi_t = 0$ for $x' < 0$ and $z' = 0$). Thus, the boundary conditions at $z' = 0$ for ϕ read

$$\begin{cases} \frac{\partial \phi}{\partial z'} = 0, & x' > H(y') \\ \phi = \Phi_{ia} e^{-i(\omega t - k_1 x' - k_2 y')}, & x' \leq H(y'). \end{cases} \quad (2.8)$$

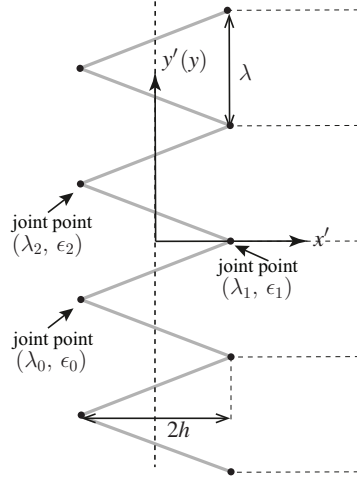


Figure 2: The schematic of serration profile.

The equation governing the second-part potential field ϕ remains unchanged, i.e.

$$\nabla^2 \phi - \frac{1}{c_0^2} \left(\frac{\partial}{\partial t} + U \frac{\partial}{\partial x'} \right)^2 \phi = 0. \quad (2.9)$$

Equation (2.9) together with the boundary conditions given in (2.8) forms a well-posed mathematical problem, and we attempt to solve it in this section.

2.2.1. Boundary-value problem

With the assumption of harmonic perturbation $\phi = \Phi(x', y', z')e^{-i\omega t}$, (2.9) reduces to

$$\beta^2 \frac{\partial^2 \Phi}{\partial x'^2} + \frac{\partial^2 \Phi}{\partial z'^2} + \frac{\partial^2 \Phi}{\partial y'^2} + 2ikM_0 \frac{\partial \Phi}{\partial x'} + k^2 \Phi = 0. \quad (2.10)$$

In order to make the boundary conditions in (2.8) independent of y' , the coordinate transformation $x = x' - H(y')$, $y = y'$, $z = z'$ is used (Roger *et al.* 2013), which leads to the following differential equation (Sinayoko *et al.* 2014; Lyu *et al.* 2015, 2016a):

$$\left(\beta^2 + H'^2(y) \right) \frac{\partial^2 \Phi}{\partial x^2} + \frac{\partial^2 \Phi}{\partial y^2} + \frac{\partial^2 \Phi}{\partial z^2} - 2H'(y) \frac{\partial^2 \Phi}{\partial x \partial y} + (2iM_0 k - H''(y)) \frac{\partial \Phi}{\partial x} + k^2 \Phi = 0, \quad (2.11)$$

where $H'(y)$ and $H''(y)$ denote the first and second derivatives of $H(y)$ with respect to y . The boundary conditions now read

$$\begin{cases} \Phi(x, y, 0) = \Phi_{ia} e^{i(k_1 x + k_2 y)} e^{ik_1 H(y)}, & x \leq 0 \\ \partial \Phi(x, y, 0) / \partial z = 0, & x > 0. \end{cases} \quad (2.12)$$

The set of equations (2.11) and (2.12) forms a linear boundary-value problem. However, unlike the governing equation for a straight leading edge (Amiet 1976a), the coefficients in (2.11) now depend on y , and therefore the standard ‘‘separation of variables’’ technique cannot be easily applied. Therefore, a Fourier expansion technique will be initially employed to eliminate the y dependency in (2.11), as explained in the following section.

2.2.2. Fourier expansion

Using both the infinite-span and serration periodicity assumptions, one can make use of the Fourier series in terms of the new coordinates (x, y, z) to expand the induced potential due to the gust interaction, as

$$\Phi(x, y, z) = \sum_{n=-\infty}^{\infty} \Phi_n(x, z) e^{ik_{2n} y}, \quad (2.13)$$

where $k_{2n} = k_2 + 2n\pi/\lambda$. Substituting this expansion into (2.11) and multiplying the resulted equation by $e^{-ik_{2n'} y}$, then integrating over y from $-\lambda/2$ to $\lambda/2$, one can readily show that

$$\begin{aligned} & \left\{ \beta^2 \frac{\partial^2}{\partial x^2} + \frac{\partial^2}{\partial z^2} + 2ikM_0 \frac{\partial}{\partial x} + (k^2 - k_{2n'}^2) \right\} \Phi_{n'} \\ & + \frac{1}{\lambda} \int_{-\lambda/2}^{\lambda/2} \sum_{n=-\infty}^{\infty} \left\{ H'^2 \frac{\partial^2}{\partial x^2} - (H'' + 2ik_{2n} H') \frac{\partial}{\partial x} \right\} \Phi_n e^{i2(n-n')\pi/\lambda y} dy = 0. \end{aligned} \quad (2.14)$$

If both $H'(y)$ and $H''(y)$ were constant within the entire wavelength, the summation over different modes in (2.14) would vanish and one would obtain an equation which only involves one mode, say n' . However, for the profile of the sawtooth serration, $H'(y)$,

is not continuous and hence $H''(y)$ is singular at the joint-points (λ_i, ϵ_i) . We use the generalized function $\delta(y)$ to describe the singularities, i.e.

$$\begin{aligned} H'(y) &= \begin{cases} \sigma_0, & \lambda_0 + m\lambda < y \leq \lambda_1 + m\lambda \\ \sigma_1, & \lambda_1 + m\lambda < y \leq \lambda_2 + m\lambda \end{cases}, \\ H''(y) &= \sum_{m=-\infty}^{\infty} (-1)^{m+1} 2\sigma \delta(x - m\lambda/2). \end{aligned} \quad (2.15)$$

where $\sigma = 4h/\lambda$ signifies the serration sharpness. As $\int_{-\infty}^{\infty} \delta(x)f(x) dx = f(0)$, the summation in (2.14) cannot be dropped, indicating that different modes are coupled together. Substituting the serration profile function and its derivatives, (2.1) and (2.15), into (2.14), and making use of the fact that $\int_{-\infty}^{\infty} f(x)\delta(x - \tau) dx = f(\tau)$, we obtain

$$\begin{aligned} &\left\{ (\beta^2 + \sigma^2) \frac{\partial^2}{\partial x^2} + \frac{\partial^2}{\partial z^2} + 2ikM_0 \frac{\partial}{\partial x} + (k^2 - k_{2n'}^2) \right\} \Phi_{n'} \\ &= -\frac{4\sigma}{\lambda} \sum_{n-n'=\text{odd}} \left(1 - \frac{k_2\lambda + 2n\pi}{(n-n')\pi} \right) \frac{\partial \Phi_n}{\partial x}. \end{aligned} \quad (2.16)$$

We can write the set of differential equations obtained above in a more compact matrix form. Using a linear operator

$$\mathcal{D} = \left\{ (\beta^2 + \sigma^2) \frac{\partial^2}{\partial x^2} + \frac{\partial^2}{\partial z^2} + 2ikM_0 \frac{\partial}{\partial x} \right\}, \quad (2.17)$$

and a vector of functions

$$\mathbf{\Phi} = (\cdots \Phi_{-n'}(x, z), \Phi_{-n'+1}(x, z), \cdots \Phi_{n'-1}(x, z), \Phi_{n'}(x, z), \cdots)^T, \quad (2.18)$$

the coupled equations in (2.16) can be written as

$$\mathcal{D}\mathbf{\Phi} = \mathbf{A}\mathbf{\Phi} + \mathbf{B} \frac{\partial \mathbf{\Phi}}{\partial x}, \quad (2.19)$$

where the symbol T in (2.18) denotes the transpose of a matrix. Matrices \mathbf{A} and \mathbf{B} denote the coefficient matrices of $\mathbf{\Phi}$ and $\partial \mathbf{\Phi} / \partial x$, respectively, and the elements A_{ml} and B_{ml} , representing the entry corresponding to mode m in row and l in column of matrix \mathbf{A} and \mathbf{B} , are given by

$$A_{ml} = (k_{2m}^2 - k^2) \delta_{ml}, \quad B_{ml} = \begin{cases} \frac{4\sigma}{\lambda} \frac{m+l+k_2\lambda/\pi}{l-m}, & m-l = \text{odd} \\ 0, & m-l = \text{even}, \end{cases} \quad (2.20)$$

where δ_{ml} represents the Kronecker delta.

The boundary condition for each mode n can be obtained by substituting the profile geometry, (2.1), into the boundary conditions, (2.12), and performing the same Fourier expansions,

$$\begin{cases} \Phi_n(x, 0) = \Phi_{ia} a_n e^{ik_1 x}, & x \leq 0 \\ \frac{\partial \Phi_n}{\partial z}(x, 0) = 0, & x > 0, \end{cases} \quad (2.21)$$

where a_n is defined as

$$a_n = \frac{1}{\lambda} \int_{-\lambda/2}^{\lambda/2} e^{ik_1 H(y)} e^{-i2n\pi/\lambda y} dy. \quad (2.22)$$

Before we attempt to solve (2.19), it is worth examining some of its important properties. The matrix \mathbf{A} is obviously a diagonal matrix and if \mathbf{B} was also diagonal, we would be able to solve each mode individually, i.e. no mode coupling. However, \mathbf{B} is not a diagonal matrix and different modes are coupled together, in the sense that Φ_n for example, appears in the governing equation of Φ_m . This means that every mode is interacting with the other modes and cannot be solved individually. Also, it can be observed from the expression of \mathbf{B} in (2.20) that the strength of the modes coupling is proportional to σ/λ . This indicates that the mode-coupling becomes stronger for sharper serrations. Obviously, the mode-coupling phenomenon fades away when the serration amplitude $2h$ is very small and the solution reduces to that of Amiet's for a straight leading-edge. Also, at very low frequencies, it is expected that the contribution of higher order modes becomes negligible compared with the 0-th mode. Thus, for the equation governing the 0-th mode, the coupling with higher modes becomes weak. One can, therefore, solve the 0-th mode individually, and calculate the potential with only the contribution of the 0-th mode. But this only works for very low frequencies or for very wide serrations. The coupling effect becomes more pronounced at high frequencies. To solve these coupled equations at relatively high frequencies, we will use an iterative procedure, which is explained in the following section.

2.2.3. Induced potential field

To obtain the induced potential field, (2.19) together with the boundary conditions in (2.21) needs to be solved. Recall a set of linear algebraic equations, it is known that its solution can be sought via the so-called iterative process (Süli & Mayers 2003). One can draw an analogy between these PDEs and the linear algebraic equations. In what follows, we shall explain the iterative procedure employed for solving our set of PDEs (Lyu *et al.* 2015, 2016b).

Substituting an assumed initial value $\Phi^{(0)}$ into the coupling term in (2.19), one can obtain

$$\mathcal{D}\Phi = \mathbf{A}\Phi + \mathbf{B}\frac{\partial\Phi^{(0)}}{\partial x}. \quad (2.23)$$

Solving (2.23) gives a new set of solutions $\Phi^{(1)}$. Replacing $\Phi^{(0)}$ in (2.23) with $\Phi^{(1)}$, we obtain a new wave equation,

$$\mathcal{D}\Phi = \mathbf{A}\Phi + \mathbf{B}\frac{\partial\Phi^{(1)}}{\partial x}. \quad (2.24)$$

Again, solving (2.24) gives a new set of solutions $\Phi^{(2)}$. Continuing this process, we obtain a solution sequence, $\Phi^{(0)}$, $\Phi^{(1)}$, $\Phi^{(2)}$, $\Phi^{(3)}$ If the sequence appears to be convergent, we manage to obtain the solution to (2.19).

The initial value $\Phi^{(0)}$ used to start the first iteration can be found by ignoring all the coupling terms, i.e. with $\mathbf{B} = 0$, and by solving each equation individually using the standard Schwarzschild technique. The solution to each equation in the uncoupled matrix equation

$$\mathcal{D}\Phi = \mathbf{A}\Phi \quad (2.25)$$

can be found as follows. Upon making use of the transformation of

$$\Phi_{n'} = \bar{\Phi}_{n'} e^{-ikM_0/(\beta^2 + \sigma^2)x}, \quad (2.26)$$

the individual equations in (2.25) reduce to

$$\left\{ (\beta^2 + \sigma^2) \frac{\partial^2}{\partial x^2} + \frac{\partial^2}{\partial z^2} + K_{n'}^2 (\beta^2 + \sigma^2) \right\} \bar{\Phi}_{n'} = 0, \quad (2.27)$$

where

$$K_{n'} = \sqrt{k^2(1 + \sigma^2) - k_{2n'}^2(\beta^2 + \sigma^2)/(\beta^2 + \sigma^2)}. \quad (2.28)$$

Making use of $X = x$ and $Z = \sqrt{\beta^2 + \sigma^2}z$ transformations, one can verify that (2.27) reduces to the standard Schwarzschild problem, as

$$\begin{cases} \left(\frac{\partial}{\partial X^2} + \frac{\partial}{\partial Z^2} + K_{n'}^2 \right) \bar{\Phi}_{n'}(X, Z) = 0, \\ \bar{\Phi}_{n'}(X, 0) = \Phi_{ia} a_{n'} e^{ik_1 X} e^{i \frac{kM_0}{\beta^2 + \sigma^2} X}, \quad X \leq 0, \\ \frac{\partial \bar{\Phi}_{n'}}{\partial X}(X, 0) = 0, \quad X > 0. \end{cases} \quad (2.29)$$

The Schwarzschild technique entails that, for $X > 0$, i.e. over the plate, the solution for (2.29) can be found from (Landahl 1961; Amiet 1976*b*, 1978)

$$\bar{\Phi}_{n'}(X, 0) = \frac{1}{\pi} \int_{-\infty}^0 \sqrt{\frac{-X}{\xi}} \frac{e^{iK_{n'}(X-\xi)}}{X-\xi} \bar{\Phi}_{n'}(\xi, 0) d\xi. \quad (2.30)$$

Evaluating (2.30) and transforming back to the physical coordinate system (x) yields the initial solution

$$\Phi_{n'}^{(0)} = -\Phi_{ia} e^{ik_1 x} a_{n'} ((1+i)E^*(\mu_{n'} x) - 1), \quad (2.31)$$

where $\Phi_{n'}^{(0)}$ is the element of vector $\mathbf{\Phi}^{(0)}$ corresponding to the n' -th mode, and

$$\begin{aligned} \mu_{n'} &= -K_{n'} + k_1 + \frac{kM_0}{\beta^2 + \sigma^2}, \\ E^*(x) &= \int_0^x \frac{e^{-it}}{\sqrt{2\pi t}} dt. \end{aligned} \quad (2.32)$$

The initial solutions obtained by ignoring all the coupling terms denote the non-coupled part of the exact solution of each mode, which implies that an n -th mode excitation ($x < 0$) produces only an n -th mode response ($x > 0$). The iteration procedure will add a coupled part to the solution of each mode.

As discussed above, by substituting $\mathbf{\Phi}^{(0)}$ into the coupling terms on the right hand side of (2.19), one obtains

$$\mathcal{D}\mathbf{\Phi} = \mathbf{A}\mathbf{\Phi} + \mathbf{B} \frac{\partial \mathbf{\Phi}^{(0)}}{\partial x}. \quad (2.33)$$

However, it should be noted that due to the inhomogeneous nature of these equations, they cannot be solved using the standard Schwarzschild technique. One therefore needs to manipulate these equations so that they change to homogeneous ones. Note that $\mathbf{\Phi}^{(0)}$ satisfies (2.25), hence, for $x \neq 0$, where $\mathbf{\Phi}^{(0)}$ is first-order continuously differentiable, the following equation holds:

$$\mathcal{D} \frac{\partial \mathbf{\Phi}^{(0)}}{\partial x} = \mathbf{A} \frac{\partial \mathbf{\Phi}^{(0)}}{\partial x}. \quad (2.34)$$

Making use of (2.34), one can show that (2.33) can be equivalently written as

$$\mathcal{D} \left(\mathbf{\Phi} + \boldsymbol{\alpha} \frac{\partial \mathbf{\Phi}^{(0)}}{\partial x} \right) = \mathbf{A} \left(\mathbf{\Phi} + \boldsymbol{\alpha} \frac{\partial \mathbf{\Phi}^{(0)}}{\partial x} \right), \quad (2.35)$$

where α is a coefficient matrix whose entries are

$$\alpha_{ml} = \frac{B_{ml}}{k_{2m}^2 - k_{2l}^2} = \begin{cases} \frac{-4h}{\pi^2(m-l)^2}, & m-l = \text{odd} \\ 0, & m-l = \text{even}. \end{cases} \quad (2.36)$$

It should be noted that for $z = 0$ (2.35) only holds when $x \neq 0$, not for $x \in \mathbf{R}$. In order to apply the Schwarzschild's technique, it must be valid over the whole domain. However, since the singularity of $\partial\Phi^{(0)}/\partial x$ only exists at $x = 0$, similar to the differentiation of $H(y)$, we may again make use of the generalized function to account for this singularity. Let $\partial\hat{\Phi}^{(0)}/\partial x$ denote the generalized differentiation, which allows the presence of generalized functions at singular point $x = 0$ but equals to $\partial\Phi^{(0)}/\partial x$ elsewhere, then equation

$$\mathcal{D}\frac{\partial\hat{\Phi}^{(0)}}{\partial x} = \mathbf{A}\frac{\partial\hat{\Phi}^{(0)}}{\partial x} \quad (2.37)$$

needs to hold for any $x \in \mathbf{R}$. The Schwarzschild technique suggests that if (2.37) does hold, then the routine application of the steps described in (2.27) to (2.31) shall recover the value of $\partial\Phi^{(0)}/\partial x$ for $x > 0$. Thus, one can show that the intended $\partial\hat{\Phi}^{(0)}/\partial x$ can indeed be found as

$$\frac{\partial\hat{\Phi}_{n'}^{(0)}}{\partial x}(x, 0) = \frac{\partial\Phi_{n'}^{(0)}}{\partial x}(x, 0) - \Phi_{ia}a_{n'}(1+i)(-\sqrt{\mu_{n'}})\sqrt{-2\pi x}\delta(x), \quad (2.38)$$

where $\partial\hat{\Phi}_{n'}^{(0)}/\partial x$ denotes the element of $\partial\hat{\Phi}^{(0)}/\partial x$ corresponding to the n' -th mode and

$$\int_{-\infty}^0 \delta(x) dx = \frac{1}{2}. \quad (2.39)$$

Now, the first iterated solution, $\Phi^{(1)}$, can be obtained by solving the following equation

$$\mathcal{D}\left(\Phi + \alpha\frac{\partial\hat{\Phi}^{(0)}}{\partial x}\right) = \mathbf{A}\left(\Phi + \alpha\frac{\partial\hat{\Phi}^{(0)}}{\partial x}\right), \quad (2.40)$$

using the steps described in (2.27) to (2.31). Continuing this iteration process gives $\Phi^{(2)}$, $\Phi^{(3)}$, \dots , and the exact solutions Φ_t after adding the initial potential field can be expressed as

$$\Phi_t(x, 0) = \mathbf{N}(x) + \mathbf{C}^{(1)}(x) + \mathbf{C}^{(2)}(x) + \mathbf{C}^{(3)}(x) + \dots, \quad (2.41)$$

where the non-coupled part is denoted by \mathbf{N} , while the coupled parts are denoted by $\mathbf{C}^{(i)}$ ($i = 1, 2, 3 \dots$). Here only the entries of \mathbf{N} and $\mathbf{C}^{(1)}$ corresponding to mode n' are presented, which are

$$N_{n'}(x) = -\Phi_{ia}e^{ik_1x}a_{n'}(1+i)E^*(\mu_{n'}x) \quad (2.42)$$

and

$$\begin{aligned} C_{n'}^{(1)}(x) = & -\Phi_{ia}e^{ik_1x}(1+i) \sum_{m=-\infty}^{\infty} \alpha_{n'm}a_m \left(ik_1 \left(E^*(\mu_{n'}x) - E^*(\mu_mx) \right) \right. \\ & \left. + \sqrt{\frac{\mu_m}{2\pi x}} \left(e^{-i\mu_{n'}x} - e^{-i\mu_mx} \right) \right) \end{aligned} \quad (2.43)$$

respectively. The result of the second iteration is rather complex and is provided in Appendix A. It is worth noting that due to the iterative nature of this solution, the function $\mathbf{C}^{(i)}$ becomes more and more complex as i increases. However, if $\mathbf{C}^{(i)}$ vanishes

sufficiently quickly, the higher orders can be dropped without causing significant errors. This appears to be the case for the frequency range of interest considered in this paper.

Substituting (2.42) and (2.43) into (2.41), a first-order approximation of the exact solution is obtained. The induced potential due to the gust interaction is finally obtained by summing the modal solutions over all different modes and transforming back to the original physical coordinate system, namely

$$\Phi_t(x', y', 0) = \sum_{n'=-\infty}^{\infty} [N_{n'} + C_{n'}^{(1)} + C_{n'}^{(2)} + \dots](x' - H(y'), 0)e^{ik_{2n'}y'}, \quad (2.44)$$

where the $N_{n'}$ and $C_{n'}^{(1)}$ functions are defined in (2.42) and (2.43) respectively, $C_{n'}^{(2)}$ can be found in the appendix and the terms in the second parenthesis are the arguments for the $N_{n'}$ and $C_{n'}^{(i)}$ ($i = 1, 2, 3, \dots$) functions.

As shown in (2.44), the induced potential field can now be expressed in terms of an infinite series. In a limiting case, when $h = 0$, all the $C_{n'}^{(i)}$ ($i = 1, 2, 3, \dots$) terms on the right hand side of (2.44) vanish, and Amiet's formulation is recovered. An interesting fact about the solution developed here is the the proportionality of $C_{n'}^{(i)} \propto h^i$ ($i = 1, 2, 3, \dots$), and thus (2.44) may be understood as a perturbation solution with respect to h . It can be shown easily that at sufficiently low frequencies, i.e. $k_1 h < \pi^2/4$, the infinite series is convergent. At higher frequencies, the series still appears to be convergent, but it can be expected that for a proper approximation, a higher truncation number and higher-order iterations will be required. The convergence issue will be further discussed in more details in Section 3.

2.2.4. Induced far-field sound pressure

As shown in the previous section, the induced potential field in the time domain can be found as

$$\phi_t(x', y', 0, t) = \sum_{n'=-\infty}^{\infty} [N_{n'} + C_{n'}^{(1)} + C_{n'}^{(2)} + \dots](x' - H(y'), 0)e^{ik_{2n'}y'} e^{-i\omega t}. \quad (2.45)$$

The pressure field is related to the velocity potential through the momentum equation, as

$$p = -\rho_0 U \left(\frac{\partial \phi_t}{\partial x'} - ik_1 \phi_t \right), \quad (2.46)$$

therefore, the pressure jump Δp across the flat plate is given by

$$\Delta p(x', y', 0, t) = 2 \sum_{n'=-\infty}^{\infty} [P_{n'}^{(0)} + P_{n'}^{(1)} + P_{n'}^{(2)} + \dots](x' - H(y'), 0)e^{ik_{2n'}y'} e^{-i\omega t}, \quad (2.47)$$

where

$$P_{n'}^{(0)}(x) = \rho_0 U \Phi_{ia} (1 + i) e^{ik_1 x} a_{n'} \sqrt{\mu_{n'}} \frac{1}{\sqrt{2\pi x}} e^{-i\mu_{n'} x} \quad (2.48)$$

and

$$P_{n'}^{(1)}(x) = \rho_0 U \Phi_{ia} (1 + i) e^{ik_1 x} \sum_{m=-\infty}^{\infty} \alpha_{n'm} a_m \left[ik_1 \frac{1}{\sqrt{2\pi x}} \left(\sqrt{\mu_{n'}} e^{-i\mu_{n'} x} - \sqrt{\mu_m} e^{-i\mu_m x} \right) - i \sqrt{\frac{\mu_m}{2\pi x}} \left(\mu_{n'} e^{-i\mu_{n'} x} - \mu_m e^{-i\mu_m x} \right) - \frac{1}{2} \sqrt{\frac{\mu_m}{2\pi x}} \frac{1}{x} \left(e^{-i\mu_{n'} x} - e^{-i\mu_m x} \right) \right]. \quad (2.49)$$

The second order solution, $P_{n'}^{(2)}(x)$, is given in the appendix. Having obtained the pressure jump across the flat plate, the far-field sound can be found using the surface pressure integral (Amiet 1975), as

$$p_f(\mathbf{x}, \omega) = \frac{-i\omega x_3}{4\pi c_0 S_0^2} \iint_s \Delta P(x', y') e^{-ikR} dx' dy', \quad (2.50)$$

where $S_0^2 = x_1^2 + \beta^2(x_2^2 + x_3^2)$ denotes the stretched distance due to the mean flow, the pressure jump has a harmonic form $\Delta P e^{-i\omega t} = \Delta p$ and the radiation distance R takes the form of

$$R = \frac{M_0(x_1 - x') - S_0}{\beta^2} + \frac{x_1 x' + x_2 y' \beta^2}{\beta^2 S_0}. \quad (2.51)$$

By substituting the solution obtained in (2.47) into (2.50), the far-field sound pressure can be found as

$$p_f(\mathbf{x}, \omega, k_2) = 2\rho_0 U \Phi_{ia} \mathcal{L}(\omega, k_1, k_2) \left(\frac{-i\omega x_3}{4\pi c_0 S_0^2} \right) \lambda \frac{\sin((N + 1/2)\lambda(k_2 - kx_2/S_0))}{\sin(\lambda/2(k_2 - kx_2/S_0))}. \quad (2.52)$$

Here, $2N + 1$ represents the number of sawteeth along the span and the non-dimensional far-field sound gust-response function \mathcal{L} is defined as

$$\mathcal{L}(\omega, k_1, k_2) = (1 + i) \frac{1}{\lambda} \left(\sum_{n'=-\infty}^{\infty} (\Theta_{n'}^{(0)} + \Theta_{n'}^{(1)} + \Theta_{n'}^{(2)} + \dots) \right) \times e^{-ik/\beta^2(M_0 x_1 - S_0)} e^{ik/\beta^2(M_0 - x_1/S_0)h}, \quad (2.53)$$

with

$$\begin{aligned} \Theta_{n'}^{(0)} &= a_{n'} \sqrt{\mu_{n'}} S_{n'n'}, \\ \Theta_{n'}^{(1)} &= \sum_{m=-\infty}^{\infty} \alpha_{n'm} a_m \left[ik_1 \left(\sqrt{\mu_{n'}} S_{n'n'} - \sqrt{\mu_m} S_{n'm} \right) \right. \\ &\quad \left. - i\sqrt{\mu_m} \left(\mu_{n'} S_{n'n'} - \mu_m S_{n'm} \right) - \sqrt{\mu_m} \left(T_{n'n'} - T_{n'm} \right) \right], \end{aligned} \quad (2.54)$$

and $\Theta_{n'}^{(2)}$ terms are provided in the Appendix. The function S_{nm} and T_{nm} in the above equations are given by

$$\begin{aligned} S_{nm} &= \sum_{j=0}^1 \frac{1}{i\kappa_{nj}} \left\{ \frac{1}{\sqrt{\eta_{Am}}} \left[e^{i\kappa_{nj}\lambda_{j+1}} E^*(\eta_{Am}(c - \epsilon_{j+1})) - e^{i\kappa_{nj}\lambda_j} E^*(\eta_{Am}(c - \epsilon_j)) \right] \right. \\ &\quad \left. - \frac{1}{\sqrt{\eta_{Bnmj}}} e^{i\kappa_{nj}(\lambda_j + (c - \epsilon_j)/\sigma_j)} \left[E^*(\eta_{Bnmj}(c - \epsilon_{j+1})) - E^*(\eta_{Bnmj}(c - \epsilon_j)) \right] \right\}, \end{aligned} \quad (2.55)$$

$$\begin{aligned} T_{nm} &= \sum_{j=0}^1 \frac{1}{i\kappa_{nj}} \left\{ \frac{-i\eta_{Am}}{\sqrt{\eta_{Am}}} \left[e^{i\kappa_{nj}\lambda_{j+1}} E^*(\eta_{Am}(c - \epsilon_{j+1})) - e^{i\kappa_{nj}\lambda_j} E^*(\eta_{Am}(c - \epsilon_j)) \right] \right. \\ &\quad \left. + \frac{i\eta_{Bnmj}}{\sqrt{\eta_{Bnmj}}} e^{i\kappa_{nj}(\lambda_j + (c - \epsilon_j)/\sigma_j)} \left[E^*(\eta_{Bnmj}(c - \epsilon_{j+1})) - E^*(\eta_{Bnmj}(c - \epsilon_j)) \right] \right\}, \end{aligned} \quad (2.56)$$

where

$$\begin{aligned}\kappa_{nj} &= k_{2n} - kx_2/S_0 + k/\beta^2(M_0 - x_1/S_0)\sigma_j, \\ \eta_{Am} &= -K_m + kM_0/(\beta^2 + \sigma^2) - k/\beta^2(M_0 - x_1/S_0), \\ \eta_{Bnmj} &= -K_m + kM_0/(\beta^2 + \sigma^2) + (k_{2n} - kx_2/S_0)/\sigma_j.\end{aligned}\quad (2.57)$$

2.3. General-gust solution

Equation (2.52) gives the far-field sound pressure induced by a single gust of form $w_i = w_{ia}e^{-i(\omega t - k_1 x' - k_2 y')}$. For a more general incoming gust given by (2.4), the induced far-field pressure can be obtained from

$$\begin{aligned}p_f(\mathbf{x}, \omega) &= 2\rho_0 \left(\frac{-i\omega x_3}{4\pi c_0 S_0^2} \right) \\ &\int_{-\infty}^{\infty} \frac{-\tilde{w}(\omega/U, k_2)}{\gamma_d(\omega/U, k_2)} \mathcal{L}(\omega, \omega/U, k_2) \lambda \frac{\sin((N+1/2)\lambda(k_2 - kx_2/S_0))}{\sin(\lambda/2(k_2 - kx_2/S_0))} dk_2.\end{aligned}\quad (2.58)$$

where p_f is the far-field sound pressure and $\gamma_d(k_1, k_2) = \sqrt{(k_1\beta + kM_0/\beta)^2 + k_2^2 - (k/\beta)^2}$. The far-field sound PSD, $S_{pp}(\mathbf{x}, \omega)$, can then be found from

$$\begin{aligned}S_{pp}(\mathbf{x}, \omega) &= \lim_{T \rightarrow \infty} \frac{\pi}{T} \overline{p_f(\mathbf{x}, \omega) p_f^*(\mathbf{x}, \omega)} \\ &= \left(\frac{\rho_0 \omega x_3}{2\pi c_0 S_0^2} \right)^2 U \\ &\int_{-\infty}^{\infty} \frac{\Phi_{ww}(\omega/U, k_2)}{|\gamma_d(\omega/U, k_2)|^2} |\mathcal{L}(\omega, \omega/U, k_2)|^2 \lambda^2 \frac{\sin^2((N+1/2)\lambda(k_2 - kx_2/S_0))}{\sin^2(\lambda/2(k_2 - kx_2/S_0))} dk_2,\end{aligned}\quad (2.59)$$

where the overbar and star denote the ensemble average and complex conjugate respectively and we have made use of the fact that (Amiet 1975)

$$\overline{w(\omega/U, k_2) w^*(\omega/U, k_2')} = \frac{L}{\pi} \delta(k_2 - k_2') \Phi_{ww}(\omega/U, k_2). \quad (2.60)$$

where Φ_{ww} denotes the wavenumber power spectral density of the incoming vertical fluctuation velocity. Equation (2.59) can be further simplified by noting that when the span d of the flat plate is large, we have

$$\lambda^2 \frac{\sin^2((N+1/2)\lambda(k_2 - kx_2/S_0))}{\sin^2(\lambda/2(k_2 - kx_2/S_0))} \sim 2\pi d \sum_{m=-\infty}^{\infty} \delta(k_2 - kx_2/S_0 + 2m\pi/\lambda), \quad (2.61)$$

and (2.59) becomes

$$\begin{aligned}S_{pp}(\mathbf{x}, \omega) &= \lim_{T \rightarrow \infty} \frac{\pi}{T} \overline{p_f(\mathbf{x}, \omega) p_f^*(\mathbf{x}, \omega)} \\ &= \left(\frac{\rho_0 \omega x_3}{2\pi c_0 S_0^2} \right)^2 U (2\pi d) \\ &\sum_{m=-\infty}^{\infty} \frac{\Phi_{ww}(\omega/U, kx_2/S_0 + 2m\pi/\lambda)}{|\gamma_d(\omega/U, kx_2/S_0 + 2m\pi/\lambda)|^2} |\mathcal{L}(\omega, \omega/U, kx_2/S_0 + 2m\pi/\lambda)|^2.\end{aligned}\quad (2.62)$$

Equation (2.62) is the fundamental equation of this paper. For the cases with the observer located on the mid-span plane, i.e. $x_2 = 0$, the sound pressure PSD reduces to

$$S_{pp}(\mathbf{x}, \omega) = (2\pi d U) \left(\frac{\rho_0 \omega x_3}{2\pi c_0 S_0^2} \right)^2 \sum_{m=-\infty}^{\infty} \frac{\Phi_{ww}(\omega/U, 2m\pi/\lambda)}{|\gamma_d(\omega/U, 2m\pi/\lambda)|^2} |\mathcal{L}(\omega, \omega/U, 2m\pi/\lambda)|^2. \quad (2.63)$$

It is worthy of pointing out that (2.63) shows that the far-field sound PSD has a linear dependence on the incoming turbulence intensities. The quantity Φ_{ww} can be obtained from various models for turbulence energy spectrum, such as but not limited to Von Karman spectrum model. Moreover, it should be emphasized that due to the assumption of a uniform mean flow and a flat plate, the effects of lifting potential flow around a realistic aerofoil are neglected in this paper. It has been shown in several papers that when the angle of attack and camber are not zero, these effects are important (Tsai & Kerschen 1990; Myers & Kerschen 1995, 1997). However, these effects would diminish as the Mach number decreases (Myers & Kerschen 1995). Consequently, the developed model in this paper should be a good approximation when at low angle of attacks and/or the Mach number is low. More importantly, though these lifting-flow effects can change the overall far-field sound spectra, it is unlikely to cause any significant changes to the predicted sound reduction, which is perhaps more important and of more practical interests.

3. Comparison with experiments

Having obtained an analytical solution for the far-field sound PSD, (2.63), we can now compare the results against the experimental data and also carry out a parametric study and investigate the effect of the serration geometry and turbulence parameters on the noise generation mechanism. As seen in (2.63), the model requires a prior knowledge of the wavenumber power spectral density of incoming vertical fluctuation velocity (Φ_{ww}). Previous experiments on leading edge noise have shown that the turbulent upwash velocity spectra can well be captured by the Von Karman energy spectrum model (Amiet 1975; Narayanan *et al.* 2015). By adopting the Von Karman energy spectrum model, Amiet (1975) showed that

$$\Phi_{ww}(k_1, k_2) = \frac{4\bar{u}^2}{9\pi k_e^2} \frac{\hat{k}_1^2 + \hat{k}_2^2}{(1 + \hat{k}_1^2 + \hat{k}_2^2)^{7/3}}, \quad (3.1)$$

where u denotes the streamwise fluctuating velocity and k_e , \hat{k}_1 and \hat{k}_2 are given by

$$k_e = \frac{\sqrt{\pi}\Gamma(5/6)}{L_t\Gamma(1/3)}, \hat{k}_1 = \frac{k_1}{k_e}, \hat{k}_2 = \frac{k_2}{k_e}, \quad (3.2)$$

where L_t is the integral scale of the turbulence and Γ is the Gamma function.

In order to validate the new model, we compare the far-field noise predictions, using (2.63), against the experimental data measured by Narayanan *et al.* (2015). The experiment was carried out for a flat plate immersed in a turbulent flow with the mean flow velocity of $U = 60$ m/s, turbulent intensity of about 2.5% and streamwise integral scale of $L_t = 0.006$ m. The flat plate had a mean-chord length of $c \approx 0.175$ m and span length of $d = 0.45$ m, fitted with a sinusoidal serration with the spanwise wavelength of $\lambda/c = 0.067$ and amplitudes of $h/c = 0.067$ (figure 3a) and $h/c = 0.167$ (figure 3b). Note that though in our model a sawtooth serration is used, for such a sharp serration, we expect the differences between the two serration profiles to be negligible. Note also that, in the experiment, the microphones were positioned outside the jet flow in the far-field. However, as pointed by Amiet (1975), the shear of the jet mean flow has no refraction effects for the observer directly above the flat plate, i.e. 90° above the flat plate leading-edge. The convection effects of the ambient mean flow, as considered in the model, have an order of β^2 for such an observer. Since the Mach number in the experiment was very low (less than 0.2), the convection effects of mean flow can be safely neglected. Therefore, we can proceed to compare the sound spectra measured in the experiment to the results

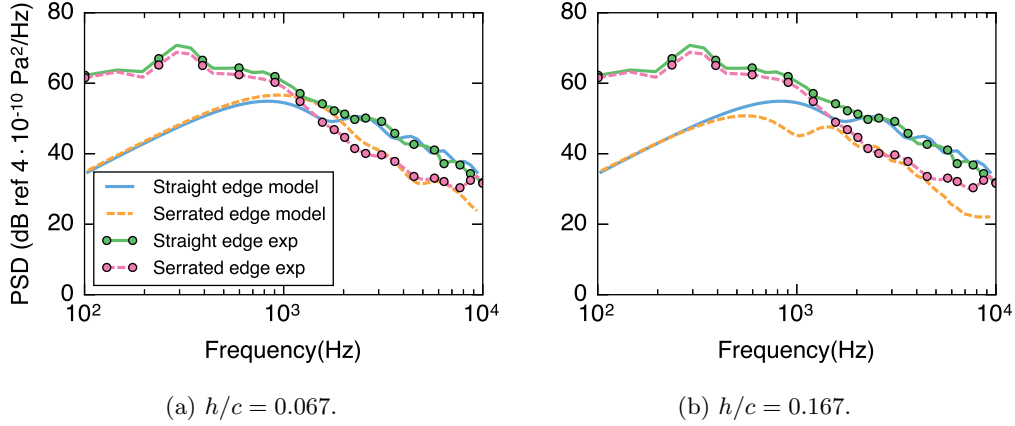


Figure 3: The validation of the second-order model, (2.63), with experimental data for the baseline (blue) and serrated (red) flat plates. The observer is at 90° above the flat plate in the mid-span plane. The Von Karman model for isotropic turbulence is used with the mean flow velocity of $U = 60$ m/s, integral length-scale of $L_t = 0.006$ m and turbulence intensity of 2.5%, as measured by Narayanan *et al.* (2015). Both serrations have a spanwise wavelength of $\lambda/c = 0.067$.

obtained in the model. As mentioned earlier, the Von Karman velocity spectrum, (3.1), was used to represent the wavenumber power spectral density of the vertical fluctuation velocity. The high level of noise at low frequencies observed in the experimental data, as mentioned by Narayanan *et al.* (2015), is believed to be due to the dominance of the open-jet wind tunnel background noise and also the grid-generated vortex shedding and its interaction with the flat plate. Therefore, the disagreement at low frequencies between the experiment and model prediction, as shown in figure 3a, is believed to be due to the dominance of jet noise. Another possible reason for such a disagreement is the perfect-coherence assumption in the streamwise direction, which will be described in details in subsequent sections. In the mid to high frequencies, however, the model provided excellent agreement with measured data. In particular, there exists a perfect match between the predicted and observed peaks of the leading edge noise of the serrated flat plate at frequencies above $f > 1000$ Hz. This suggests that the model captures the essential physics and gives accurate prediction of the noise from plates and aerofoil fitted with leading-edge serrations. Predictions under the same flow condition for a much sharper serrations, i.e. $\lambda/c = 0.067$ and $h/c = 0.167$, are presented in figure 3b. It can be seen that sharper serrations are more effective in reducing leading edge noise, which has been demonstrated by both the experimental data and model predictions. The agreement between the model and experiments continues to be very good in the frequency range where leading edge noise is dominant. The slight mismatch at high frequencies ($f > 7$ kHz) for the serrated case is likely to be caused by other noise mechanisms present in the experiment, as seen in the experimental data, such as the trailing-edge noise.

The results presented in figure 3 were calculated using the second-order solutions, but we have not yet examined the rate of convergence of the solution in (2.63). To demonstrate that the second-order solution can provide a sufficiently accurate solution, we present the predicted sound pressure spectra for the first validation case (figure 3a) using the 0th, 1st and 2nd-order solutions. The results are shown in figure 4. Though a difference of up to 5 dB can be observed between the 0th- and 1st-order solutions, the difference between

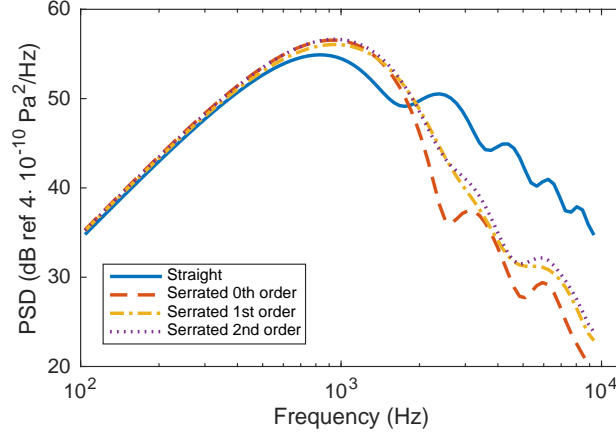


Figure 4: The convergence of the 0th, 1st and 2nd order solutions.

the 1st- and 2nd-order solutions is uniformly less than 1 dB over the entire frequency range of interest. This suggests that the second-order solution should serve as a good approximation for the serration cases considered in this study and over the frequency range of interest.

4. Discussions

4.1. Effects of serration geometry

In this section, we carry out a parametric numerical evaluation of the model to study the effects of serration geometry and Mach number on leading edge noise. Since we are primarily interested in the effects of serration geometry and flow convective effects, we shall use the same chord-length and incoming turbulence statistical quantities as in the preceding section, i.e. $c \approx 0.175$ m, $L_t = 0.006$ m and turbulent intensity of 2.5%. Results will be presented for the far-field sound power spectra at 90° above the flat plate in the mid-span plane.

Results in figure 5a presents the far-field sound pressure level for a flat plate with wide serrations, i.e. $\lambda = 3L_t$, with different amplitudes, i.e. h from $1/3L_t$ to $3L_t$, in a relatively low Mach number flow of $M_0 = 0.1$. Note here, we use “wide” to describe the serrations which have longer wavelength λ compared to those shown subsequently. Similarly, “sharp” serrations have been used to describe serrations with small value of λ . It is clear from the results that serrations of $h = 1/3L_t$ have virtually no effects on reducing the far-field sound. This is expected since a leading edge with wide and short serrations will act very similar to a straight edge. On the other hand, serrations with relatively large root-to-tip amplitude, $h = L_t$, start to reduce the noise at high frequencies, as shown by the dash-dotted line in figure 5a. The use of longer serrations, i.e. $h = 3L_t$, is shown to result in significant reduction of the far-field noise, even at low frequencies.

Figure 5b shows the results for a flat plate with leading-edge serration wavelength of $\lambda = L_t$. The effect of varying the serration amplitude (h) on the reduction of turbulence interaction noise is similar to those observed before. However, an important difference compared with the wider serration case with $\lambda = 3L_t$, see figure 5a, is that an area of noise increase appears at low frequencies for short serrations (small h). The reason of such noise increases at low frequencies will be discussed later in Section 4.3. Results are also

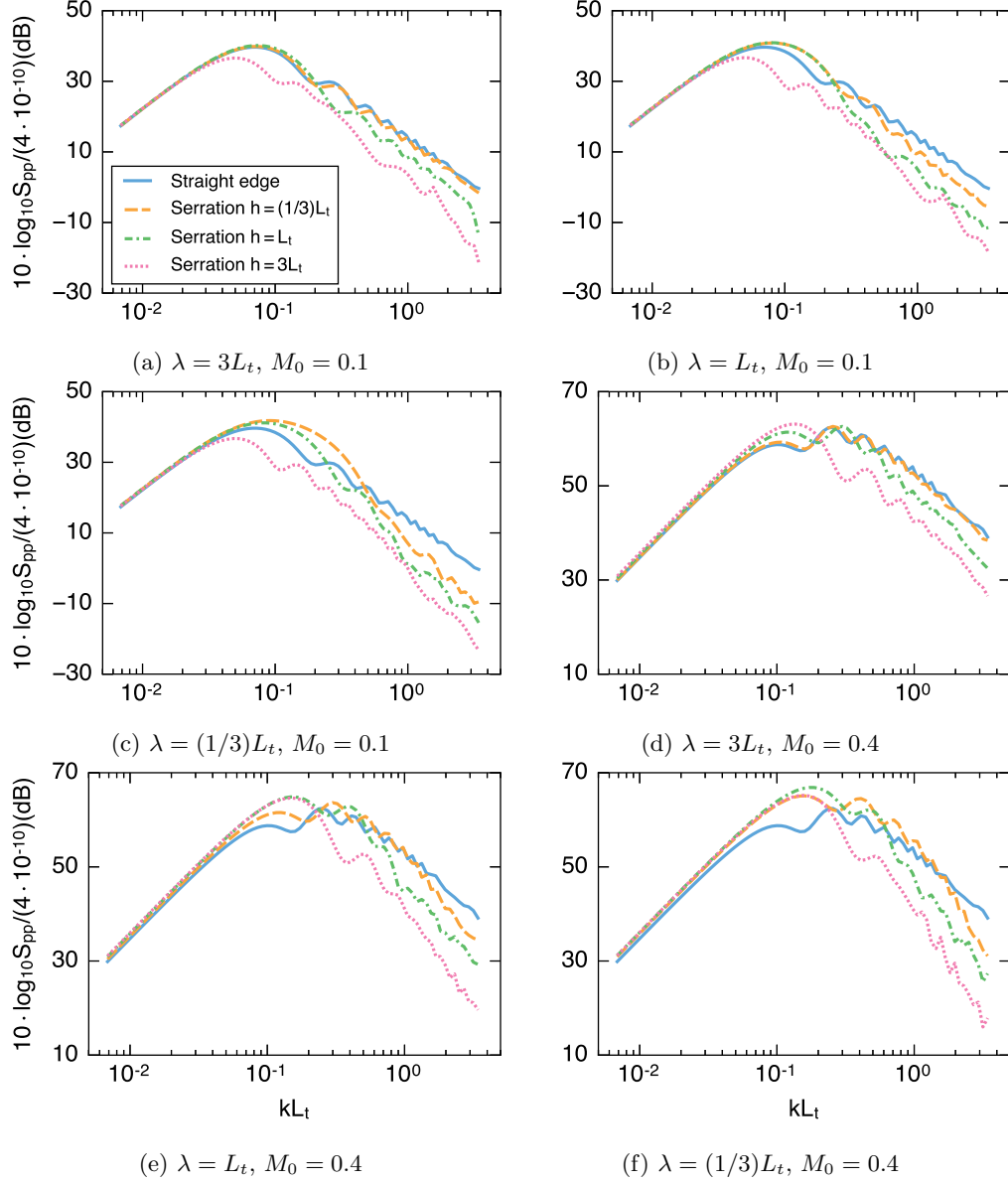


Figure 5: The effects of varying h and λ on far-field sound spectrum. The observer is located at 90° above the flat plate in the mid-span plane. The Von Karman model for isotropic turbulence is used with the integral length-scale of $L_t = 0.006\text{m}$ and turbulence intensity of 2.5%, as measured by [Narayanan *et al.* \(2015\)](#). The flat plate has a mean chord length of $c = 0.175\text{ m}$ and span length of $d = 0.45\text{ m}$.

presented for very sharp serrations ($\lambda = 1/3L_t$), see figure 5c. The noise increase observed at low frequencies for serrations with small h is now more pronounced. However, one can see that so long as the serration is long enough, the noise increase disappears completely and that using sharp serrations (small λ) results in more effective sound reduction at high frequencies compared with the wide serrations. In summary, the results suggest that in

order to suppress the leading edge noise, the serration wavelength λ has to be sufficiently small and the root-to-tip amplitude has to be large.

The effect of flow convective effects, particularly at high Mach numbers, can also be studied using the new model. As mentioned earlier, since the formulations are based on Amiet's leading-edge noise theory, where the convection effects of the uniform mean flow has properly accounted for, the new model should suffer no constraints caused by high-speed mean flow convection effects. Therefore the model can be used for higher Mach numbers (when the uniform mean flow assumption is permissible). This capability is particularly important as most of the experimental data available are collected at low Mach numbers of up to 0.23 (Narayanan *et al.* 2015). Figures 5d to 5f present the far-field noise from a flat plate in a turbulent flow with the Mach number of $M_0 = 0.4$. Results are presented for wide ($\lambda = 3L_t$) to sharp ($\lambda = 1/3L_t$) serrations. In general, the results show the same trends as before, that is greater noise reduction can be achieved using sharp serrations and that the use of wide and small leading edge serrations can lead to noise increase at about $kL_t = 0.1$. The level of noise increase for shallow serrations (large λ and small h) has been observed to increase significantly with Mach number.

4.2. Directivity

The effects of leading edge serrations on far-field noise directivity have also been investigated. In this section, we shall study the effects of a specific leading edge serration on the directivity patterns at different non-dimensionlized frequencies (kL_t) and Mach numbers ($M_0 = 0.1$ and 0.4). From Section 4.1, we see that in order to achieve significant noise reduction, the serration wavelength λ has to be sufficiently small and the serration amplitude $2h$ has to be sufficiently large. However, it is also found that when λ is too small, e.g. $\lambda = (1/3)L_t$, there is also a large noise increase at intermediate frequencies. Therefore, in practical applications, the serration profile with $\lambda = L_t$ and $h = 3L_t$ is preferred. In this section, we choose this geometry to study the effects of serration on directivity at different frequencies and Mach numbers. As before, the flat plate has a mean-chord length of $c = 0.175$ m and span length $d = 0.45$ m. Also, the incoming flow turbulence intensity is set to 2.5% and integral length-scale is taken as $L_t = 0.006$ m. Results are presented at different acoustic wavenumbers kL_t , corresponding to the convective wavenumbers of $k_1L_t = 0.2, 0.5, 1, 2, 5$ and 10 (see figures 6).

Figure 6a shows the directivity patterns for both the straight and serrated edges at the frequency of $kL_t = 0.02$ ($k_1L_t = 0.2$). At such low frequencies, the serrations have no effects on the radiated sound. Slight noise reduction only appears when frequency increases to $kL_t = 0.05$ ($k_1L_t = 0.5$), as shown in figure 6b. Further increasing the frequency results in more effective sound reduction, as shown in figure 6c. It is interesting to note that at mid-frequencies, i.e. $kL_t = 0.2$ and 0.5 ($k_1L_t = 2$ and 5), greater noise reduction is obtained for observer locations closer to the trailing edge side of the flat plate, i.e. $\theta = 0^\circ$, see figures 6d and 6e. At higher frequency $kL_t = 1$ ($k_1L_t = 10$), significant noise reduction can be achieved at all radiation angles and the noise reduction at $\theta = 90^\circ$ reaches up to 10 dB. Another interesting phenomenon observed is the significant changes to the directivity pattern of the radiated noise. As seen for the low frequencies, i.e. $kL_t = 0.02$ and 0.05, the introduction of leading edge serrations does not particularly change the dipolar shape of the radiated sound field. However, at higher frequencies, the cardioid shape of leading edge noise is changed to a more tilted dipolar shape, as seen in figures 6c to 6f.

The far-field noise directivity results at Mach number of $M_0 = 0.4$ are presented in figure 7. Figure 7a shows the directivity results at $kL_t = 0.08$ ($k_1L_t = 0.2$). Compared to figure 6a for $M_0 = 0.1$, we see a slight noise increase at low frequencies. This is consistent

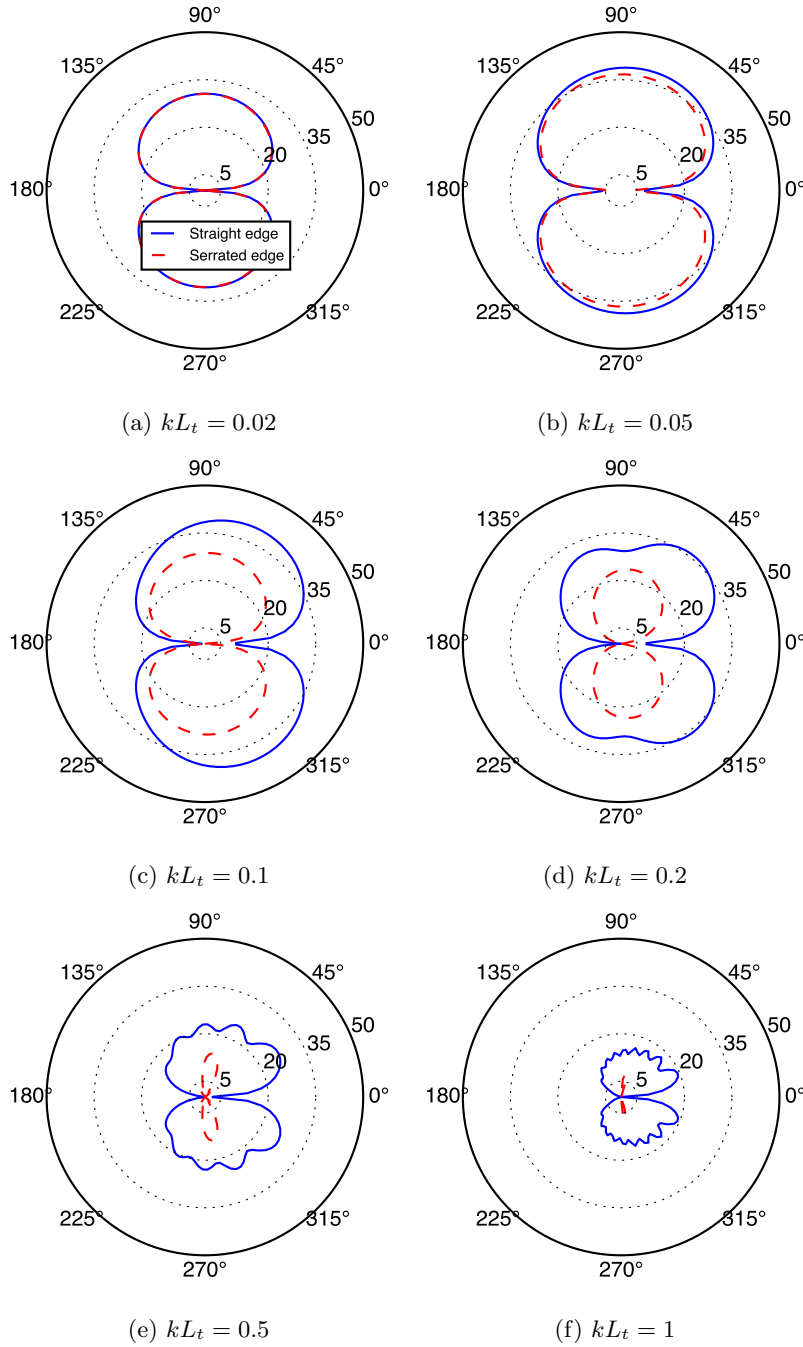


Figure 6: The directivity of leading edge noise for both straight and serrated edges at Mach number $M_0 = 0.1$ in the mid-span plane. The Von Karman model for isotropic turbulence is used in the analytical model with the turbulent intensity of 2.5% and length-scale of $L_t = 0.006$ m. Results are presented at different frequencies (kL_t), corresponding to convective wavenumbers of $k_1 L_t = 0.2, 0.5, 1, 2, 5$ and 10.

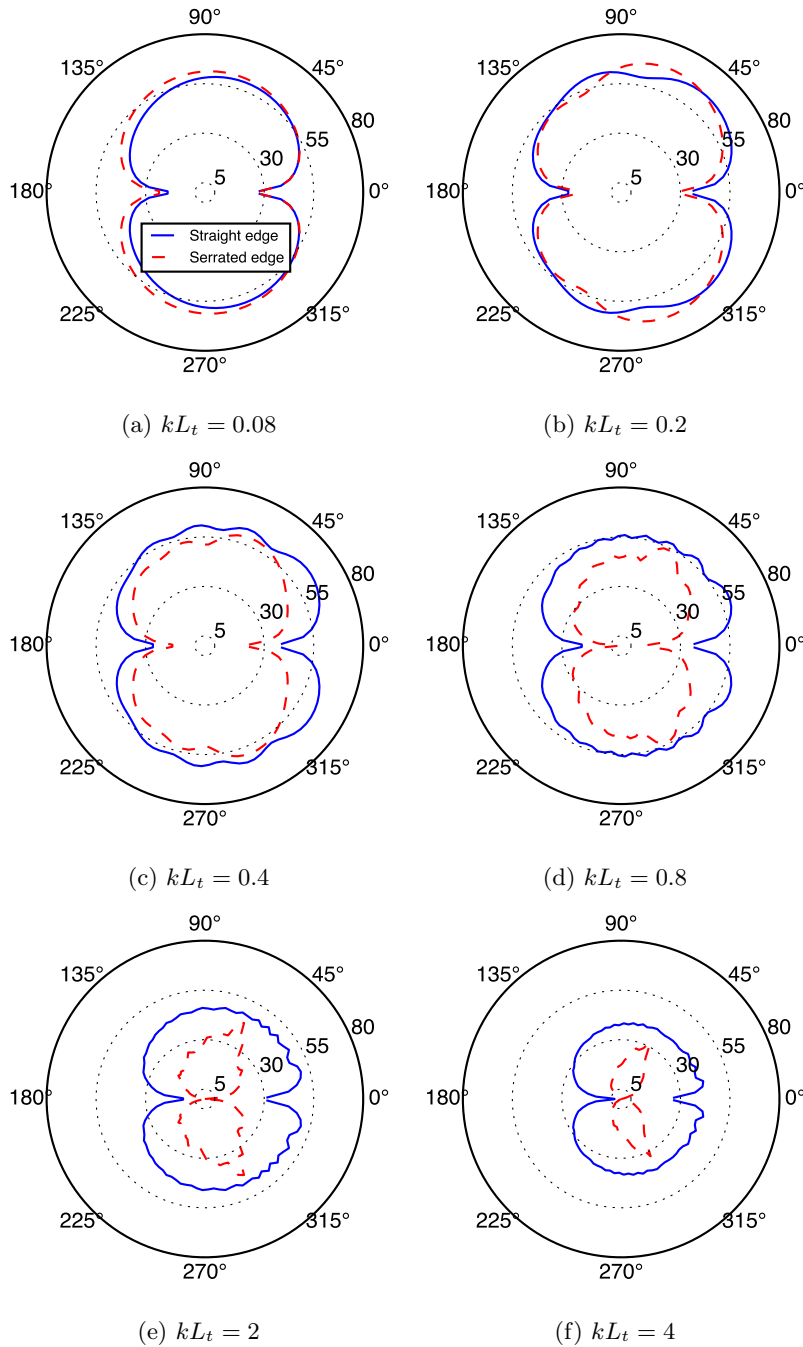


Figure 7: The directivity of leading edge noise for both straight and serrated edges at Mach number $M_0 = 0.4$ in the mid-span plane. The Von Karman model for isotropic turbulence is used in the analytical model with the turbulent intensity of 2.5% and length-scale of $L_t = 0.006$ m. Results are presented at different frequencies (kL_t), corresponding to convective wavenumbers of $k_1 L_t = 0.2, 0.5, 1, 2, 5$ and 10.

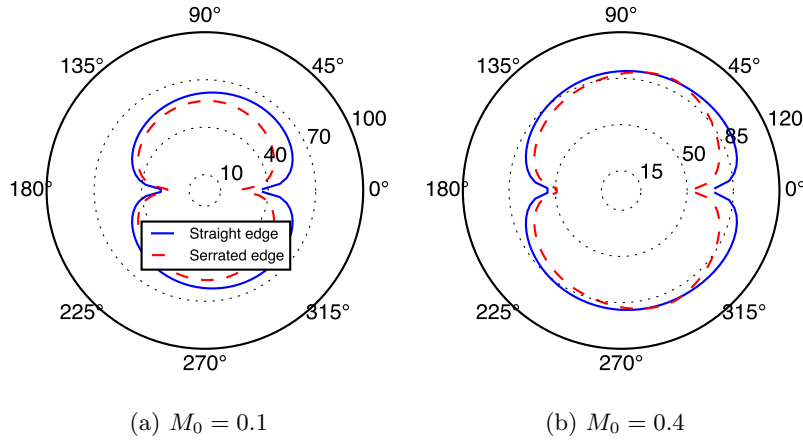


Figure 8: The leading edge far-field noise OASPL directivity patterns for both straight and serrated leading edges in the mid-span plane. The serration used has a wavelength of $\lambda = L_t$ and half root-to-tip amplitude of $h = 3L_t$ and the incoming flow has a turbulent intensity of 2.5% and integral length-scale of $L_t = 0.006\text{m}$

with our findings in the preceding section, i.e. noise increase is more pronounced at high Mach numbers. This noise increase persists at around 90° above and below the plate for frequencies up to $kL_t = 0.2$ ($k_1L_t = 0.5$), as shown in figure 7b. The use of leading edge serrations at $kL_t = 0.4$ ($k_1L_t = 1$), however, leads to noise reduction at all angles, as can be seen in figure 7c. Figures 7d to 7f show the directivity patterns at $kL_t = 0.8, 2$ and 4 , respectively, corresponding to convective wavenumber of $k_1L_t = 2, 5$, and 10 . As before, results here confirm that the leading edge serrations are more effective at high frequencies and that the use of leading edge serration changes the far-field noise directivity from a cardioid shape to a tilted dipole.

In addition to the sound pressure level at different frequencies, the overall sound pressure level (OASPL) results can also provide some insight into the total sound energy radiated at different angles and the effects of leading edge serrations. This also provides an opportunity to better understand the effectiveness of the leading edge serration as most of the OASPL results obtained experimentally are contaminated due to the strong low frequency background jet noise contribution. The OASPL results here are obtained by integrating the sound power of the frequency range of $kL_t = 0.02$ to 2 (for $M_0 = 0.1$) and $kL_t = 0.04$ to 4 (for $M_0 = 0.4$). As in the previous section, the serration used has a wavelength of $\lambda = L_t$ and half root-to-tip amplitude of $h = 3L_t$ and the incoming flow has a turbulent intensity of 2.5% and integral length-scale of $L_t = 0.006\text{m}$. Results are presented at Mach numbers of $M_0 = 0.1$ and 0.4 , see figures 6 and 7. Results have shown that the use of leading edge serration can result in significant reduction of the OASPL of up to 5-10 dB. It has also been observed that the leading edge serration are more effective at low Mach numbers and small polar angles, i.e. downstream towards to the plate's surface. This was also observed in the far-field SPL results in figures 6 and 7 at mid to high frequencies.

4.3. Noise reduction mechanism

Inspection of the equations developed in Section 2 shows that in order for the leading edge serration treatment to be effective, two geometrical criteria must be met. The detailed derivations are not provided for the sake brevity, and interested readers can refer to

the paper by the authors (Lyu *et al.* 2016b) on noise from aerofoils with trailing edge serrations. The two geometrical criteria are (1) $\omega h/U \gg 1$ and (2) $\omega h_e/U \gg 1$, where the effective half root-to-tip length h_e is defined by $h_e = \sigma l_{y'}/2$ and $l_{y'}$ is the spanwise correlation length defined by

$$l_{y'}(\omega) = \frac{1}{R(\omega, 0)} \int_{-\infty}^{\infty} R(\omega, y') dy',$$

where $R(\omega, y')$ is the spanwise two-point correlation of the incoming turbulent velocity. Using Von Karman model, Amiet (1975) showed that $l_{y'}(\omega)$ can be obtained as

$$l_{y'}(\omega) = \frac{16L_t}{3} \left(\frac{\Gamma(1/3)}{\Gamma(5/6)} \right)^2 \frac{(\omega/Uk_e)^2}{(3 + 8(\omega/Uk_e)^2) \sqrt{1 + (\omega/Uk_e)^2}}. \quad (4.1)$$

It may seem somewhat unexpected to obtain the dependence of the sound reduction on the spanwise correlation length. A careful inspection of (2.59) reveals that this dependence originates from the wavenumber power spectral density $\Phi_{ww}(\omega, k_2)$ in (2.59). The inverse Fourier transformation of $\Phi_{ww}(\omega, k_2)$ over k_2 yields the two-point cross spectrum $R(\omega, y')$. The first criterion is consistent with the findings in the numerical work by Lau *et al.* (2013) and some experimental data available for different leading edge serrations (Chaitanya *et al.* 2016). The second criterion, although less discussed in recent works, is an important condition and relates the serration geometry to the structure of the incoming turbulence.

As shown in other numerical and experimental works, the main cause of noise reduction is due to the destructive sound interferences caused by the serration. In that sense, the noise reduction mechanism is very similar to that of trailing edge serration, as previously discussed by Lyu *et al.* (2016b). The better understanding of the destructive sound interference phenomenon may help us better explain the physical implications of the two above-mentioned criteria. The first condition $\omega h/U \gg 1$ is to ensure that a complete phase variation (of minimum 2π) of the scattered pressure along the serration edge is achieved. At low frequencies, this requires the serration amplitude $2h$ to be large in order to achieve significant sound reduction, as only a large value of h can ensure a complete phase variation of the scattered pressure field along the serration edge. For the cases when the serration amplitude h is not large enough, there would be little variation of the scattered pressure, i.e. in-phase radiation along the edge. This can result in noise increase at low frequencies, as observed in figures 3 and 5, which is due to the fact that the wetted edge by an in-phase pressure field for the serrated edge is longer than that of the straight-edge. It should be noted that in this paper we assume that the incoming turbulence is frozen. This would imply a perfect spatial correlation in the streamwise direction for the upwash velocity field. For serrations with large h , the assumption of perfect streamwise correlation of the turbulence becomes inappropriate, and therefore the condition developed may not hold. This might explain why a noise increase is predicted in figure 3a while this did not happen in experimental results. However, for mid- to high-frequency regimes this assumption should serve as a good approximation, as demonstrated by both figure 3a and 3b. The importance of the second criterion is also easy to understand. Since the noise reduction relies on the destructive interference, the scattered pressure needs to be correlated. $\omega h_e/U \gg 1$ effectively ensures this, hence makes pressure cancellation due to phase variation possible.

To clearly demonstrate the effect of the $\omega h/U$ criterion, we present the scattered pressure on the upper surface of the flat plate at fixed $\omega h_e/U = 7$ in figure 9. To better understand the effect of sound interference, the x' - and y' -axis are normalized by the

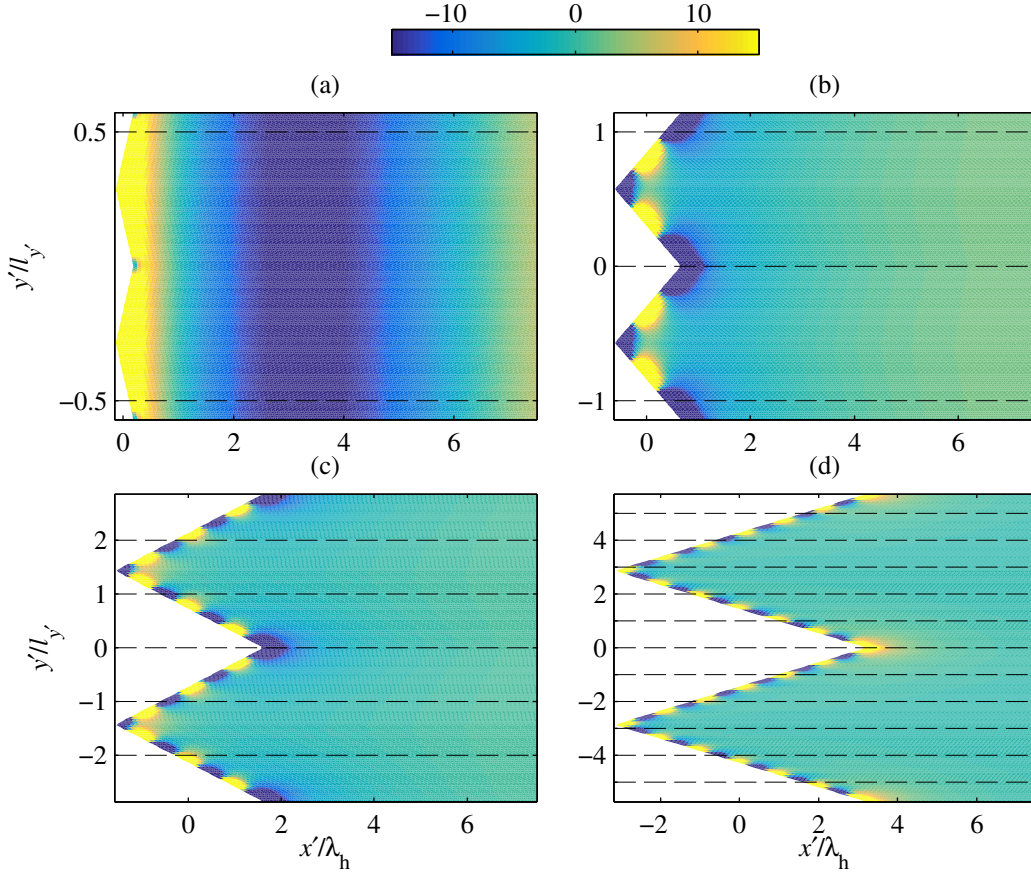


Figure 9: The effects of varying $\omega h/U$ on the scattered surface pressure at a fixed frequency and $\omega h_e/U = 7$: a) $\omega h/U = 1$; b) $\omega h/U = 4$; c) $\omega h/U = 10$; d) $\omega h/U = 20$. The color shows the normalized scattered pressure on the upper surface of the flat plate. The vertical axis shows the spanwise coordinate normalized by the spanwise correlation length and the horizontal axis shows the streamwise coordinate normalized by the hydrodynamic wavelength.

hydrodynamic wavelength ($\lambda_h = 2\pi U/\omega$) and spanwise correlation length ($l_{y'}$). The distance between the adjacent y' -grid lines shown in figure 9 are used to show the spanwise correlation length $l_{y'}$. When $\omega h/U = 1$, as can be seen from figure 9(a), little phase variation is induced along and near the leading edge in the spanwise direction. This suggests little sound reduction occurs due to destructive interference. As $\omega h/U$ increases to 4, as shown in figure 9(b), phase variation of the scattered pressure near the leading edge become noticeable. Further increasing $\omega h/U$ to 10, we see from figure 9(c) that significant sound reduction can be achieved due to the strong phase variation near the leading edge in the spanwise direction. Figure 9(d) shows that pressure distribution when $\omega h/U = 20$. It is evident that when $\omega h_e/U$ is fixed, the number of pressure crests and troughs within $l_{y'}$ is fixed at sufficiently large value of $\omega h/U$ (see figures 9(b) to (d)). The effects of $\omega h_e/U$ are similarly shown in figure 10, where $\omega h/U$ is fixed at 10 while $\omega h_e/U$ varies from 1 to 10. From figure 10(a) to (d) the scattered pressure patterns are virtually the same. However, the phase variation of the surface pressure within the

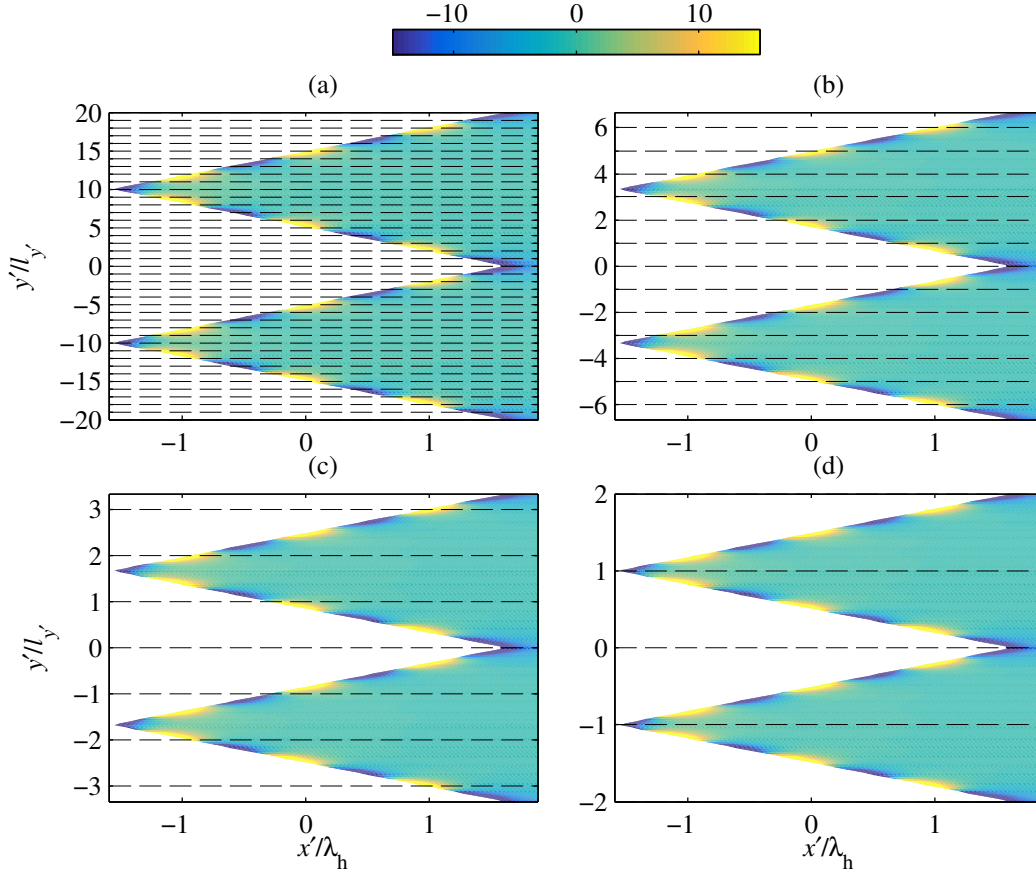


Figure 10: The effects of varying $\omega h_e/U$ on the scattered surface pressure at a fixed frequency and $\omega h/U = 10$: a) $\omega h_e/U = 1$; b) $\omega h_e/U = 3$; c) $\omega h_e/U = 6$; d) $\omega h_e/U = 10$. The color shows the normalized scattered pressure on the upper surface of the flat plate. The vertical axis shows the spanwise coordinate normalized by the spanwise correlation length and the horizontal axis shows the streamwise coordinate normalized by the hydrodynamic wavelength.

spanwise correlation length $l_{y'}$ is very different. In figure 10(a) we see that within the length of $l_{y'}$ (between adjacent y' -grid lines), the phase variation of pressure is negligible. Since the destructive interference can only occur within $l_{y'}$, little sound reduction can be expected in this case. On the other hand, figure 10(c) and (d) show that a sufficient number of crests and troughs appearing within the length $l_{y'}$, leading to effective noise reduction due to the destructive interference within $l_{y'}$. Figures 9 and 10 clearly show that in order to achieve significant sound reduction, both $\omega h/U \gg 1$ and $\omega h_e/U \gg 1$ have to be satisfied.

5. Conclusions and future work

A new mathematical model is developed in this paper with the aim to predict the sound radiated from the interaction of an incoming turbulent flow with a flat plate with serrated leading edge. By making use of the Fourier expansion and the Schwarzschild

techniques, the power spectral density of the far-field sound is related to the wavenumber spectral density of the incident velocity field. The model is based on Amiet's approach and is therefore valid even for high Mach number applications where leading edge noise is a common problem. The comparisons with experimental data have shown an excellent agreement and this suggests that the model can capture the essential physics of the noise generation and reduction mechanisms and can provide accurate prediction of the noise from serrated leading edges. A thorough parametric study has been carried out using the new model and the effects of leading edge serration geometry and incoming turbulent flow characteristics on far-field noise at different Mach numbers have been studied. It has been found that in order to achieve significant noise reduction, the serration amplitude $2h$ has to be sufficiently large compared to the hydrodynamic wavelength in the streamwise direction. More specifically, the condition of $\omega h/U \gg 1$ needs to be satisfied. The spanwise correlation length also plays an important role in achieving effective noise reduction. In order to achieve significant noise reduction, a second condition of $\omega h_e/U \gg 1$ has to be satisfied, which ensures that scattered pressure is correlated for a possible destructive interference to occur. It has also been shown that leading edge serration can effectively reduce the far-field noise at even high Mach numbers. However, larger serrations might be needed especially in the relatively low frequency regimes. From the far-field noise directivity patterns, it has been observed that more sound reduction occurs for observer locations near the trailing edge side of the flat plate and that the noise directivity at high frequencies changes from the cardioid shape to a tilted dipole-like pattern. The mathematical model developed in this paper has shown that the destructive sound interference is the primary noise reduction mechanism, especially in the mid- to high-frequency regime where leading edge noise is most effectively reduced using serrations. Further work is needed to address the issue of perfect coherence for the incoming turbulence in the streamwise direction, which might not be an accurate assumption at low frequencies.

Appendix

5.1. Second iterated results

The 0- and 1-order solutions of $\Phi_t(x, 0)$ are given by (2.42) and 2.43, respectively, in Section 2. The 2-order solution is given by $C_{n'}^{(2)}(x)$ as follows

$$\begin{aligned}
C_{n'}^{(2)}(x) = & -\Phi_{ia}(1+i)e^{ik_1x} \sum_{m=-\infty}^{\infty} \left\{ \beta_{n'm}(ik_1)^2(E^*(\mu_{n'}x) - E^*(\mu_mx)) \right. \\
& + (\beta_{n'm}ik_1 + \gamma_{n'm}i(k_1 - \mu_m)) \sqrt{\frac{\mu_m}{2\pi x}} (e^{-i\mu_{n'}x} - e^{-i\mu_mx}) \\
& \left. - \frac{\gamma_{n'm}}{2} \left(\sqrt{\frac{\mu_m}{2\pi x}} \frac{1}{x} (e^{-i\mu_{n'}x} - e^{-i\mu_mx}) + i(\mu_{n'} - \mu_m) \sqrt{\frac{\mu_m}{2\pi x}} e^{-i\mu_{n'}x} \right) \right\},
\end{aligned} \tag{5.1}$$

where

$$\begin{aligned}
\beta_{ln} &= \sum_{m=-\infty}^{\infty} (\alpha_{ln}a_m - B_{lm}/(k_{2l}^2 - k_{2n}^2)a_n)\alpha_{nm}, \\
\gamma_{ln} &= \sum_{m=-\infty}^{\infty} (\alpha_{ln}a_m\sqrt{\mu_m/\mu_n} - B_{lm}/(k_{2l}^2 - k_{2n}^2)a_n)\alpha_{nm}.
\end{aligned}$$

Similarly, $P_{n'}^{(2)}(x)$ can be expressed as

$$\begin{aligned}
P_{n'}^{(2)}(x) &= \rho_0 U \Phi_{ia} (1+i)e^{ik_1 x} \\
&\sum_{m=-\infty}^{\infty} \left\{ \beta_{n'm} (ik_1)^2 \frac{1}{\sqrt{2\pi x}} (\sqrt{\mu_{n'}} e^{-i\mu_{n'} x} - \sqrt{\mu_m} e^{-i\mu_m x}) \right. \\
&\quad - (\beta_{n'm} ik_1 + \gamma_{n'm} i(k_1 - \mu_m)) \left[i \sqrt{\frac{\mu_m}{2\pi x}} (\mu_{n'} e^{-i\mu_{n'} x} - \mu_m e^{-i\mu_m x}) + \right. \\
&\quad \quad \left. \left. \frac{1}{2} \sqrt{\frac{\mu_m}{2\pi x}} \frac{1}{x} (e^{-i\mu_{n'} x} - e^{-i\mu_m x}) \right] \right. \\
&\quad + \gamma_{n'm} \left[i \frac{1}{2} \sqrt{\frac{\mu_m}{2\pi x}} \frac{1}{x} (\mu_{n'} e^{-i\mu_{n'} x} - \mu_m e^{-i\mu_m x}) + \right. \\
&\quad \quad \left. \frac{1}{2} \frac{3}{2} \sqrt{\frac{\mu_m}{2\pi x}} \frac{1}{x^2} (e^{-i\mu_{n'} x} - e^{-i\mu_m x}) + \right. \\
&\quad \quad \left. \left. i \frac{(\mu_{n'} - \mu_m)}{2} (i\mu_{n'} \sqrt{\frac{\mu_m}{2\pi x}} e^{-i\mu_{n'} x} + \frac{1}{2} \sqrt{\frac{\mu_m}{2\pi x}} \frac{1}{x} e^{-i\mu_{n'} x}) \right] \right\}. \quad (5.2)
\end{aligned}$$

Finally, $\Theta_{n'}^{(2)}$ can be found as

$$\begin{aligned}
\Theta_{n'}^{(2)} &= \sum_{m=-\infty}^{\infty} \left\{ \beta_{n'm} (ik_1)^2 (\sqrt{\mu_{n'}} S_{n'n'} - \sqrt{\mu_m} S_{n'm}) \right. \\
&\quad - (\beta_{n'm} ik_1 + \gamma_{n'm} i(k_1 - \mu_m)) \left[i \sqrt{\mu_m} (\mu_{n'} S_{n'n'} - \mu_m S_{n'm}) + \right. \\
&\quad \quad \left. \sqrt{\mu_m} (T_{n'n'} - T_{n'm}) \right] \\
&\quad + \gamma_{n'm} \left[i \sqrt{\mu_m} (\mu_{n'} T_{n'n'} - \mu_m T_{n'm}) + \sqrt{\mu_m} (V_{n'n'} - V_{n'm}) \right. \\
&\quad \quad \left. \left. + i \frac{(\mu_{n'} - \mu_m)}{2} (i\mu_{n'} \sqrt{\mu_m} S_{n'n'} + \sqrt{\mu_m} T_{n'n'}) \right] \right\}, \quad (5.3)
\end{aligned}$$

where function V_{nm} is given by

$$\begin{aligned}
V_{nm} &= \sum_{j=0}^1 \left\{ \frac{1}{\sigma_j} e^{i\kappa_{ij}(\lambda_j + (c - \epsilon_j)/\sigma_j)} \times \right. \\
&\quad \left[\frac{1}{\sqrt{2\pi}(c - \epsilon_j)} e^{-i\eta_{Bnmj}(c - \epsilon_j)} - \frac{1}{\sqrt{2\pi}(c - \epsilon_{j+1})} e^{-i\eta_{Bnmj}(c - \epsilon_{j+1})} \right] \\
&\quad + \frac{1}{i\kappa_{nj}} \left(\frac{-i\eta_{Am}}{\sqrt{\eta_{Am}}} \left[e^{i\kappa_{nj}\lambda_{j+1}} E^*(\eta_{Am}(c - \epsilon_{j+1})) - e^{i\kappa_{nj}\lambda_j} E^*(\eta_{Am}(c - \epsilon_j)) \right] \right) + \\
&\quad \quad \frac{i\eta_{Bnmj}}{\sqrt{\eta_{Bnmj}}} e^{i\kappa_{nj}(\lambda_j + (c - \epsilon_j)/\sigma_j)} \times \\
&\quad \quad \left. \left[E^*(\eta_{Bnmj}(c - \epsilon_{j+1})) - E^*(\eta_{Bnmj}(c - \epsilon_j)) \right] \right\}. \quad (5.4)
\end{aligned}$$

Acknowledgments

The first author (BL) wishes to gratefully acknowledge the financial support provided by the Cambridge Commonwealth European and International Trust and China Scholarship Council. The second author (MA) would like to acknowledge the financial support of the Royal Academy of Engineering.

REFERENCES

- ALLAMPALLI, V., HIXON, R., NALLASAMY, M. & SAWYER, S. D. 2009 High-accuracy large-step explicit Runge–Kutta (HALE-RK) schemes for computational aeroacoustics. *Journal of Computational Physics* **228** (10), 3837–3850.
- AMIET, R. K. 1975 Acoustic radiation from an airfoil in a turbulent stream. *Journal of Sound and Vibration* **41** (4), 407–420.
- AMIET, R. K. 1976a High frequency thin-airfoil theory for subsonic flow. *AIAA Journal* **14** (8), 1076–1082.
- AMIET, R. K. 1976b Noise due to turbulent flow past a trailing edge. *Journal of Sound and Vibration* **47** (3), 387–393.
- AMIET, R. K. 1978 Effect of the incident surface pressure field on noise due to turbulent flow past a trailing edge. *Journal of Sound and Vibration* **57**, 305–306.
- ATASSI, H. M., FANG, J. & PATRICK, S. 1993 Direct calculation of sound radiated from bodies in nonuniform flows. *Journal of Fluids Engineering* **115** (4), 573–579.
- BROOKS, T. F., POPE, D. S. & MARCOLINI, M. A. 1989 Airfoil self-noise and prediction. NASA reference publication 1218. NASA.
- BUSHNELL, D. M. & MOORE, K. J. 1991 Drag reduction in nature. *Annual Review of Fluid Mechanics* **23**, 65–79.
- CHAITANYA, P., NARAYANAN, S., JOSEPH, P. & KIM, J. W. 2016 Leading edge serration geometries for significantly enhanced leading edge noise reductions. In *Proceedings of the 22nd AIAA/CEAS Aeroacoustics Conference*. American Institute of Aeronautics and Astronautics, AIAA 2016-2736.
- CURLE, N. 1955 The influence of solid boundaries upon aerodynamic sound. *Proceedings of the Royal Society A: Mathematical, Physical and Engineering Sciences* **231**, 505–514.
- DEVENPORT, W. J., STAUBS, J. K. & GLEGG, S. A. L. 2010 Sound radiation from real airfoils in turbulence. *Journal of Sound and Vibration* **329** (17), 3470–3484.
- FISH, F. E. & BATTLE, J. M. 1995 Hydrodynamic design of the humpback whale flipper. *Journal of Morphology* **225**, 51–60.
- FISH, F. E., HOWLE, L. E. & MURRAY, M. M. 2008 Hydrodynamic flow control in marine mammals. *Integrative and Comparative Biology* **48** (6), 788–800.
- GILL, J., ZHANG, X. & JOSEPH, P. 2013 Symmetric airfoil geometry effects on leading edge noise. *The Journal of the Acoustical Society of America* **134** (4), 2669–2680.
- GOLDSTEIN, M. E. 1978 Unsteady vortical and entropic distortions of potential flows round arbitrary obstacles. *Journal of Fluid Mechanics* **89**, 443–468.
- GOLDSTEIN, M. E. & ATASSI, H. 1976 A complete second-order theory for the unsteady flow about an airfoil due to a periodic gust. *Journal of Fluid Mechanics* **74**, 741–765.
- GRAHAM, J. M. R. 1970 Similarity rules for thin aerofoils in non-stationary subsonic flows. *Journal of Fluid Mechanics* **43** (04), 753–766.
- HANSEN, K. L., KELSO, R. M. & DALLY, B. B. 2011 Performance variations of leading-edge tubercles for distinct airfoil profiles. *AIAA Journal* **49** (1), 185–194.
- HIXON, R., MANKBADI, R. R., SCOTT, J. R., SAWYER, S. & NALLASAMY, M. 2006 Application of a nonlinear computational aeroacoustics code to the gust-airfoil problem. *AIAA Journal* **44** (2), 323–328.
- JOHARI, HAMID, HENoch, C. W., CUSTODIO, DERRICK & LEVSHIN, ALEXANDRA 2007 Effects of leading-edge protuberances on airfoil performance. *AIAA journal* **45**, 2634–2642.
- K. HANSEN, R. KELSO & DOOLAN, C. 2012 Reduction of flow induced airfoil tonal noise using leading edge sinusoidal modifications. *Acoustics Australia* **40** (3), 172–177.
- KIM, J. W., HAERI, S. & JOSEPH, P. F. 2016 On the reduction of aerofoil-turbulence interaction noise associated with wavy leading edges. *Journal of Fluid Mechanics* **792**, 526–552.

- KOVASZNAV, L. S. G. 1953 Turbulence in supersonic flow. *Journal of the Aeronautical Sciences* **20** (10), 657–674.
- LANDAHL, M. 1961 *Unsteady Transonic Flow*. New York: Pergamon Press, Inc.
- LAU, A. S. H., HAERI, S. & KIM, J. W. 2013 The effect of wavy leading edges on aerofoil-gust interaction noise. *Journal of Sound and Vibration* **332** (24), 6234–6253.
- LYU, B., AZARPEYVAND, M. & SINAYOKO, S. 2015 A trailing-edge noise model for serrated edges. In *Proceedings of the 21st AIAA/CEAS Aeroacoustics Conference*. American Institute of Aeronautics and Astronautics, AIAA 2015-2362.
- LYU, B., AZARPEYVAND, M. & SINAYOKO, S. 2016a Noise prediction for serrated leading-edges. In *Proceeding of 22th AIAA/CEAS Aeroacoustics Conference*. American Institute of Aeronautics and Astronautics, AIAA 2016-2740.
- LYU, B., AZARPEYVAND, M. & SINAYOKO, S. 2016b Noise prediction for serrated trailing edges. *Journal of Fluid Mechanics* **793**, 556–588.
- MIKLOSOVIC, D. S. & MURRAY, M. M. 2004 Leading-edge tubercles delay stall on humpback whale (megaptera novaeangliae) flippers. *Physics of Fluids* **16** (5).
- MYERS, M. R. & KERSCHEN, E. J. 1995 Influence of incidence angle on sound generation by airfoil interacting with high-frequency gusts. *Journal of Fluid Mechanics* **292**, 271–304.
- MYERS, M. R. & KERSCHEN, E. J. 1997 Influence of camber on sound generation by airfoils interacting with high-frequency gusts. *Journal of Fluid Mechanics* **353**, 221–159.
- NARAYANAN, S., CHAITANYA, P., HAERI, S., JOSEPH, P., KIM, J. W. & PLACSEK, C. 2015 Airfoil noise reductions through leading edge serrations. *Physics of Fluid* **27** (025109).
- PATERSON, R. W. & AMIET, R. K. 1976 Acoustic radiation and surface pressure response of an airfoil due to incident turbulence. *Tech. Rep.*. CR-2733, NASA, Washington, DC.
- PEDRO, H. T. C. & KOBAYASHI, M. H. 2008 Numerical study of stall delay on humpback whale flippers. In *Proceedings of the 46th AIAA Aerospace Sciences Meeting and Exhibit*. American Institute of Aeronautics and Astronautics, AIAA 2008-584.
- ROGER, M. & CARAZO, A. 2010 Blade-geometry considerations in analytical gust-airfoil interaction noise models. In *Proceedings of the 16th AIAA/CEAS Aeroacoustics Conference*. American Institute of Aeronautics and Astronautics, AIAA 2010-3799.
- ROGER, M. & MOREAU, S. 2005 Back-scattering correction and further extensions of Amiet's trailing-edge noise model. Part 1: theory. *Journal of Sound and Vibration* **286** (1-2), 477–506.
- ROGER, M., SCHRAM, C. & SANTANA, L. D. 2013 Reduction of airfoil turbulence-impingement noise by means of leading-edge serrations and/or porous materials. In *Proceedings of the 19th AIAA/CEAS Aeroacoustics Conference*. American Institute of Aeronautics and Astronautics, AIAA 2013-2108.
- SEARS, W. R. 1941 Some aspects of non-stationary airfoil theory and its practical application. *Journal of the Aeronautical Sciences* **8**, 104–108.
- SINAYOKO, S., AZARPEYVAND, M. & LYU, B. 2014 Trailing edge noise prediction for rotating serrated blades. In *Proceeding of 20th AIAA/CEAS Aeroacoustics Conference*. American Institute of Aeronautics and Astronautics, AIAA 2014-3296.
- SÜLLI, E. & MAYERS, D. 2003 *An introduction to numerical analysis*. Cambridge University Press.
- TSAI, C. T. & KERSCHEN, E. J. 1990 Influence of airfoil nose radius on sound generated by gust interactions. *AIAA Journal* (90-3912).
- TURNER, J. M. & KIM, J. W. 2016 Towards understanding aerofoils with dual-frequency wavy leading edges interacting with vortical disturbances. In *Proceedings of the 22nd AIAA/CEAS Aeroacoustics Conference*. American Institute of Aeronautics and Astronautics, AIAA 2016-2951.